applied sciences

MDPI

Review

A Review of Pore Structure Characterization Methods Utilized in Oil and Gas Carbonate Formations

Tao Long [1,2], Yankun Sun [1,2,*], Peng Peng [1,2], Liangchang Zhou [1,2], Tianyu Sun [1,2], Chengjie Jin [1,2], Junyuan Ding [1,2], Xu Zhang [3] and Bowen Chen [4]

1 Hubei Procincial Key Laboratory of Oil and Gas Exploration and Development Theory and Technology, China University of Geosciences, Wuhan 430074, China; 13098344527@163.com (T.L.); m15871424921@163.com (P.P.); clzhou0719@163.com (L.Z.); 16696170036@163.com (T.S.); jinchengjie2004@163.com (C.J.); 17860715221@163.com (J.D.)
2 Key Laboratory of Tectonics and Petroleum Resources, Ministry of Education, Wuhan 430074, China
3 Geological Exploration Technology Institute of Anhui Province, Energy Exploration Center, Hefei 230041, China; xuzhangcags@163.com
4 College of Zijin Geology and Mining, Fuzhou University, Fuzhou 350116, China; chen-bowen940321@fzu.edu.cn
* Correspondence: sunyankun@cug.edu.cn

Abstract

Pore structure characterization is crucial for understanding fluid flow in porous media, including oil and gas reservoirs, aquifers, and geologic formations. Carbonate formations, prevalent in oil and gas reservoirs, pose challenges due to their complex pore structure. This review summarizes diverse methods reported in the literature to characterize the pore structure of carbonate formations. Emphasizing the need for multiple methods and scales, the paper discusses pore-throat classification, imaging techniques (X-ray CT, SEM, and NMR), and pore network modeling. These methods help identify typical pore-throat types and structural features, which commonly exhibit irregular shapes and poor connectivity, thus influencing fluid flow behavior. Pore network modeling elucidates structural heterogeneity and its impact on fluid flow. These insights are vital for oil and gas production and groundwater management, providing a comprehensive understanding of fluid flow in porous media.

Keywords: carbonate reservoirs; pore structure; characterization methods; fluid flow

1. Introduction

Global carbonate-hosted oil and gas resources are remarkably abundant and have emerged as primary targets for development in the future energy sector [1–6]. The variability of diagenetic processes and sedimentary environment constitutes a primary driver behind the intricate pore structure of carbonate rocks [7–10]. The pore structure mainly refers to the morphology, size, distribution and connectivity [11]. Mineralogical variations in carbonate rocks increase the uncertainty of conventional porosity logs (density and neutron) in matrix density and porosity models, mainly due to the density differences between calcite and dolomite, and changes in formation hydrogen index caused by clay and bound water [12]. Presence of secondary porosity, especially vugs (large pores), challenges the reliability of permeability models in carbonate rocks [13]. The complexity of these depositional environments creates a high level of heterogeneity and sudden changes in pore sizes within the same geological unit [14,15]. Therefore, carbonate rocks are characterized

Academic Editor: Tiago Filipe da Silva Miranda

Received: 16 March 2026
Revised: 4 May 2026
Accepted: 12 May 2026
Published: 22 May 2026

 https://doi.org/10.3390/app16115225

by strong heterogeneity and complex pore structures and mineralogical variability, which significantly complicate conventional petrophysical measurements such as porosity and permeability [16–21].

In light of the importance of carbonate oil and gas resources for human survival, a better understanding of the heterogeneous properties of carbonates is of great significance for exploring resource development [11]. Influenced by the interaction between chemistry and diagenesis, the porosity evolution of carbonate rocks becomes more complicated [22–25]. The fluid flow properties of the system are significantly affected by the following three key characteristics of microporous regions: elevated pore density, increased complexity of pore geometry, and enhanced pore connectivity [26–32]. Choquette and Pray (1970) identified recognized different pore types in carbonate reservoirs based on their genesis, size, and fluid flow characteristics [33]. Skalinski and Kenter (2015) [34] classified the carbonate pore classification methods in the literature into the following three types: geology, rock physics, and reservoir engineering disciplines. Despite the valuable contributions of previous studies, the characterization of complex pore structures in carbonate reservoirs remains of great significance, primarily due to the wide pore size distribution of intricate pore networks and the varying degrees of connectivity within these networks [35–38].

Variations in pore sizes and throat apertures can exert a significant influence on fluid-flow characteristics in carbonate formations [39–42]. Thus, a reliable characterization of pore types and pore-network properties can enhance assessment of petrophysical properties in carbonate formations [43]. Therefore, the primary objective of this study is to review various advanced methods that have been applied for the full-scale characterization of pore structures in carbonate formations, thereby providing insights into the development of carbonate rock characterization technologies.

Several studies have explored the pore structure of carbonate formations, along with different pore types and their corresponding size, shape, and associated throats. Gundogar et al. (2016) [11] used SEM, image analysis, and mercury porosimetry to analyze the geometrical and topological properties of carbonate pores, including porosity, pore body and throat sizes, coordination number, shape factor, aspect ratio, and their distributions. Wang et al. (2012) [44] used SEM (scanning electron microscope) images of carbonates at different resolutions to construct 3D digital rock models at both macro- and microscales, and used pore analysis tools to generate pore network models and perform flow calculations. Oyewole et al. (2015) [45] combined MICP (mercury injection capillary pressure) measurements, micro-CT (Micro-computed Tomography) images, and well logs to characterize the pore structure and size distribution of carbonates, and to classify rocks based on petrophysical properties and mineralogy. Zhenpeng et al. (2015) [46] used Macro-CT, micro-CT, and Nano-CT (Nano-computed Tomography) to study the pore structure of core samples at millimeter, micrometer, and nanometer scales, and used SEM to identify pore size, type, and origin. Yao et al. (2015) [47] employed SEM to scan carbonate thin section images with varying pixel and used multi-resolution image analysis and a percolation model to study the connectivity of vugs, interpores, and intrapores.

Each characterization technique offers distinct advantages in practice. SEM and CT imaging are well-suited for observing complex pore geometries, diagenetic characteristics, and multiscale pore types. MICP provides more dependable quantitative results for pore-throat size distributions. NMR enables non-destructive evaluation of pore connectivity and fluid mobility. Nevertheless, these methods all face inherent limits in applicable scales and test conditions. SEM only captures two-dimensional surface information. MICP cannot reliably measure nanoscale pores and may damage samples. CT is constrained by resolution and cost, while NMR cannot directly present real pore morphologies. For this reason, no single method can fully describe the strong heterogeneity of carbonate reservoirs.

In addition to studies focusing on domestic basins, extensive research has been conducted on carbonate reservoirs worldwide.

Due to the fact that almost all major carbonate reservoirs in the Middle East are typical Arabian platform carbonate rocks, a large number of scholars have studied the structural characteristics of carbonate rocks in the region. Xiao et al. (2014) [48] characterized the micropore structure of low-permeability carbonate reservoirs in the Middle East via constant-rate mercury penetration. They identified that reservoir permeability is dominated by throat size, and the pore-throat ratio rises sharply with decreasing permeability. Carbonate cores present a more balanced contribution of throats to permeability than sandstone, leading to lower development difficulty; Yue et al. (2024) [49] characterized the pore structure and predicted permeability of Middle Eastern Y-type carbonate reservoirs using high-pressure mercury intrusion and X-ray CT. They verified that core classification improves prediction accuracy, and their proposed bimodal Gaussian PSD model is more suitable for complex carbonate reservoirs after gas slip correction; Mahmoud et al. (2023) [50] investigated Middle Eastern carbonate reservoirs using digital rock physics (DRP) and multi-scale X-ray CT. They characterized pore structures and predicted permeability via the lattice Boltzmann method (LBM). The results show that the simulated permeability is consistent with laboratory measurements, verifying DRP as an effective method for characterizing heterogeneous carbonate reservoirs.

As an important global oil and gas producing area, Brazil's research on carbonate reservoirs mainly focuses on the pre-salt Cretaceous carbonate rock system in the Santos Basin. Basso et al. (2021) [51] investigated the pre-salt lacustrine carbonate reservoirs in the Santos Basin, Brazil, using core observation, thin-section analysis, CT scanning and NMR testing. They analyzed sedimentary facies, pore structure and diagenetic modifications and concluded that diagenesis controls reservoir quality more strongly than sedimentary facies; Iraji et al. (2023) [52] characterized the pre-salt lacustrine carbonate reservoirs of the Barra Velha Formation in the Santos Basin, Brazil, by integrating well logging, core analysis, micro-CT and thin-section observations. They used the K-means algorithm combined with traditional rock physics methods to classify reservoirs into four types (RRT1 to RRT4) based on their physical properties, from good to poor.

The characterization of pore structure in carbonate reservoirs in north Africa is a core scientific issue in oil and gas exploration and development. Radwan et al. (2021) [53] performed multi-scale characterization on tight Eocene carbonate reservoirs in the Gulf of Suez Basin, Egypt, using core observations, thin sections, NMR measurements and well logging data. Their results show that fracture pores and moldic pores are the dominant pore types and interparticle pores mainly occur in the basal interval. Baouche et al. (2021) [54] analyzed the petrophysical and geomechanical properties of late Cretaceous carbonate reservoirs in the southeastern Constantine Basin, Algeria. They divided the reservoirs into the following two rock types: RRT-I with nano-micropores and poor reservoir quality, and RRT-II with mesopores and good reservoir performance.

Razavifar et al. (2021) [55] from Imperial College London compared MIP, NMR, μCT and gas injection to characterize the pore structure of carbonate rocks. They found that high-resolution μCT (5 μm voxel size) yields the most accurate porosity closest to the gas porosimetry measurement, while low-resolution μCT severely underestimates porosity. NMR provides a reliable pore-size distribution consistent with high-resolution μCT, and MIP only roughly characterizes the throat-size distribution.

Integrated studies from these leading institutions have established standard workflows for multiscale pore characterization in world-class carbonate reservoirs, strongly supporting the comprehensiveness of this review.

These studies contribute valuable insights into the pore structure of carbonate formations and its influence on petrophysical properties. While these studies provide significant contributions, there exists a research gap in the form of a consolidated review that specifically focuses on the diverse methods for pore structure characterization in oil and gas carbonate formations. This review aims to address this gap by synthesizing findings from various studies, highlighting the nuances of each method, and providing a comprehensive overview.

To ensure the comprehensiveness and representativeness of this review, a systematic literature search was conducted using Web of Science, ScienceDirect, Springer, and IEEE Xplore databases. The main keywords included carbonate reservoirs, pore structure, characterization methods, SEM, CT, NMR, MICP, and pore network modeling. The literature published from 2010 to 2025 was primarily selected, focusing on high-quality journal articles with complete experimental data and clear methodological descriptions. Only studies closely related to carbonate pore structure characterization were included to maintain the focus and reliability of this review.

An understanding of pore structural intricacies in carbonate formations is crucial for optimizing oil and gas production and managing groundwater resources efficiently. This review seeks to bridge the existing knowledge gap within the literature and contribute to the broader understanding of fluid flow in porous media within the context of carbonate formations.

2. Methods for Characterization of Pore Structure

This section outlines the core methods used to characterize pore structures in carbonate formations, along with their key features and limitations.

The characterization of pore structure in rock samples is important for understanding the physical and chemical properties of these materials. There are several methods that have been developed for this purpose, including scanning electron microscopy (SEM), nuclear magnetic resonance (NMR), mercury intrusion porosimetry (MIP), high-pressure mercury intrusion (HPMI), and gas sorption [43,56–63]. The SEM and MIP methods are commonly used to evaluate pore type, geometry and connectivity [64–67]. Furthermore, quantitative characterization of pore-size distribution, pore volume, and specific surface area can be achieved through a combination of low-pressure gas adsorption, NMR, mercury injection capillary pressure (MICP), and small-angle neutron scattering (SANS) [68–70].

As a powerful instrument, the scanning electron microscope (SEM) delivers high-resolution images of materials and is widely used in various areas of science and industry [71–73]. In the characterization of pore structure, the role of scanning electron microscopy (SEM) is to scan the sample surface point by point after the electron beam emitted by the electron gun is incident on it. The secondary electron and backscattered electron signals generated are converted and displayed on the screen as 2D images of the sample surface characteristics, thereby obtaining the pore morphology, size, and mineral composition of the rock sample (Figure 1) [74].

The application of SEM in carbonate rocks differs significantly from other rock types. Sandstone, mudstone and other reservoirs often focus on the characteristics of particles and intergranular pores, while carbonate rocks have diverse mineral compositions, strong diagenesis, complex pore types, and often develop nanoscale pore throats. Therefore, when using scanning electron microscopy technology to analyze carbonate rocks, more emphasis is placed on identifying intergranular pores, dissolution pores, bioclastic structures, and diagenetic features such as recrystallization and dolomitization, with higher requirements for imaging resolution and magnification.

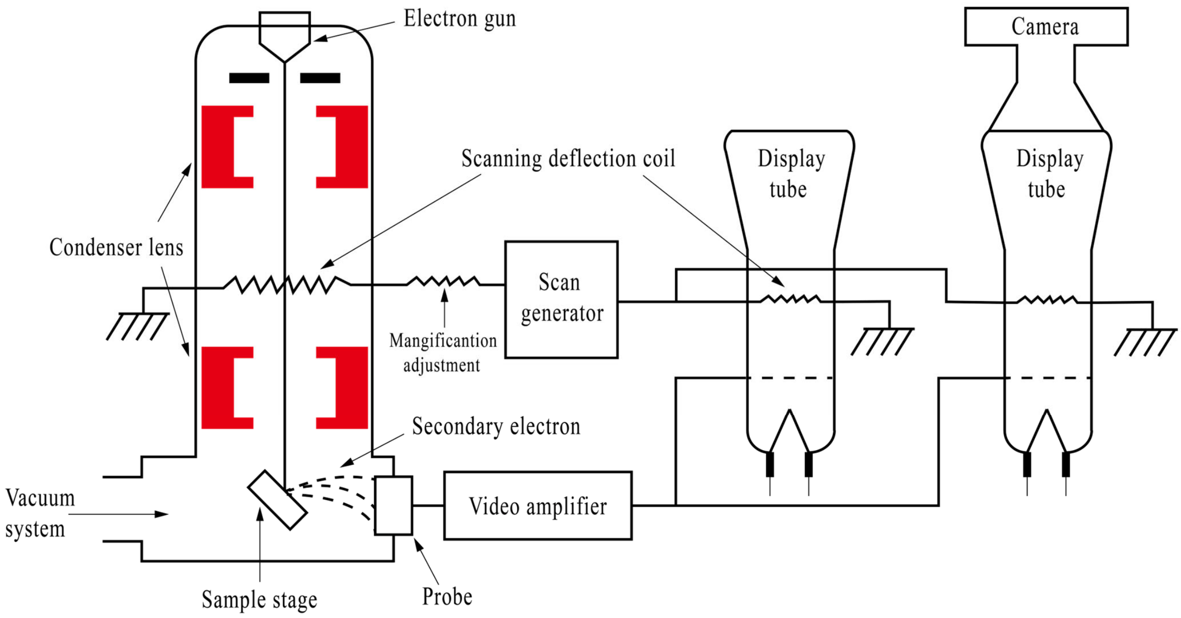

Figure 1. Schematic diagram of the working principle of SEM. Adapted from [68].

However, SEM cannot provide direct quantitative data for pore-size distribution, but can support quantitative analysis through image segmentation and processing [43,47]. For example, SEM cannot directly measure "volumetric porosity" but can measure "area porosity". It should be noted that SEM area porosity refers to the ratio of pore area to total area, which is not equal to volumetric porosity. This parameter is often represented in SEM ϕ (% area) format.

In the characterization of pore structure, NMR technology mainly obtains pore structure information by measuring the transverse relaxation time ($T2$) of hydrogen nuclei in pore fluids [75–81]. The transverse relaxation time ($T2$) exhibits high sensitivity to pore structure and is given by the following mathematical formula:

$$\frac{1}{T_2} = \rho_2 \frac{S}{V} + \frac{1}{T_{2b}} + \frac{D(G\gamma TE)^2}{12} \tag{1}$$

$$G = G_{external} + G_{internal} \tag{2}$$

$$G_{internal} \approx B_0 \frac{\Delta\chi}{\mathrm{r}} \tag{3}$$

where ρ_2 is the surface relaxivity, μs/m; T_{2b} is bulk relaxation time; D is the free diffusion coefficient for the fluid, μs/cm^2; γ is the gyromagnetic ratio; TE is the echo spacing of the measurement sequence, ms; S/V is the surface area to volume ratio (specific surface area) of the pores, μs^{-1}; G is the magnetic field gradient, which includes the external and interior magnetic field gradient, Gauss/cm; B_0 is the applied magnetic field strength, Gauss/cm; r refers to the distance from the magnetic field changes, m; and $\Delta\chi$ is the susceptibility difference between rock matrix particles and pore fluid, 10^{-6} SI.

NMR is more commonly applied to carbonate rocks due to their lack of magnetic minerals that could interfere with the pore fluid signal. The specific surface area can reflect the pore size distribution in carbonate rock formations. According to Equation (1), T_2 is inversely proportional to the specific surface area (S/V). For spherical pores, the surface-to-volume ratio S/V can be simplified as follows:

$$\frac{S}{V} = \frac{3}{r} \tag{4}$$

where r is the pore radius. By substituting into the NMR relaxation model, the T_2–pore radius conversion relationship is obtained:

$$r = 3\rho_2 T_2 \tag{5}$$

This equation establishes the direct quantitative link between NMR T_2 relaxation time and actual pore size, which is widely used for pore-size distribution conversion in carbonates. The smaller the pore size, the larger the specific surface area and the shorter the measured T_2. Therefore, NMR transforms the "pore topology" into "fluid relaxation time", and then uses relaxation time to infer pore size, porosity, connectivity, and mobility [82–85]. The NMR method can cover a pore size measurement range encompassing micropores, mesopores, and macropores, with its main measurement objects being open pores or those connected to the outside [86–88].

Mercury intrusion porosimetry (MIP), a widely used quantitative analytical method in reservoir studies for effectively characterizing pore structures, involves injecting mercury into a rock sample and measuring the pressure required to force the mercury into the pores [89–91]. Mercury intrusion porosimetry (MIP) is a reliable method; however, it is not suitable for certain types of samples, such as those with macropores or complex pore structures. Additionally, it can be time-consuming and only capable of analyzing interconnected/effective porosity [92–94].

$$P = -\frac{2\gamma\cos\theta}{r} \tag{6}$$

where P is applied pressure; γ is the surface tension of the mercury; θ is the contact angle; and r is the pore radius. Because γ is 0.480 N/m for mercury, Equation (1) can be simplified to:

$$r = \frac{750}{P} \tag{7}$$

where the unit of the pressure is MPa, the unit of the pore radius is nm.

The HPMI measurement serves as a rapid and efficient technique for analyzing the pore structure characteristics and ascertaining the distribution of pore-throat sizes [47]. Many researchers have conducted studies based on the combination of HPMI curves with the permeability and porosity of rocks to classify pore types and reservoir types of rock samples. At present, HPMI measurement is one of the most commonly used methods for characterizing the pore-throat size distribution of 3–500 µm [95,96]. When the invasion pressure is high, it may cause small pores to close, reducing the test result accuracy [97]. Thus, it is not suitable for characterizing nanoscale pores, predominantly under 50 nm in size, in tight reservoirs [98].

Gas sorption is a method that involves measuring the amount of gas that is absorbed by a sample at different pressures. The Brunauer–Emmett–Teller (BET) model is widely used to calculate the specific surface area, based on the core equation:

$$\frac{p/p_0}{V(1-p/p_0)} = \frac{1}{\mathrm{V}_m C} + \frac{(C-1)(p/p_0)}{\mathrm{V}_m C} \tag{8}$$

where p/p_0 is the relative pressure, V is the adsorbed gas volume, V_m is the monolayer adsorption volume, and C is the BET constant related to adsorption energy. The Barrett–Joyner–Halenda (BJH) method is further applied to determine pore size distribution from desorption data, using the following relationship:

$$V_t = \sum \frac{{r_t}^2}{{r_p}^2} \Delta V_d \tag{9}$$

where V_t is the pore volume, r_t is the meniscus radius during desorption, r_p is the actual pore radius, and ΔV_d is the volume change in desorbed gas. This can be used to determine the pore size distribution and total porosity of the sample. Gas sorption is a fast and accurate method, but it is not suitable for all types of samples, such as those with large or complex pores, and it requires specialized equipment [99,100]. The advantage of the use of gas adsorption relies on its relatively low cost and its ability to provide useful information regarding pore architecture and a description of the pore-size distribution [101–103].

Micro-CT analysis is a method of computerized tomography (CT) that uses digital geometry processing to generate a three-dimensional image of the interior of a rock core. This technique is useful for providing information about the pore structure, filling distribution, particle surface structure, and physical property parameters of rock cores. One advantage of micro-CT analysis is that it is a non-destructive method for imaging the open and closed pores inside rock samples [104,105]. However, micro-CT analysis also has some disadvantages. One major disadvantage is its high cost, which can be up to 20 times more expensive than other methods such as MIP. Additionally, the detection range of micro-CT is limited by its poor resolution, which can only reach the micron level. This means that only pores within a certain size range can be detected, and the maximum horizon is around 1000 to 2000 times larger than the resolution [106,107].

Another disadvantage of micro-CT analysis is that it requires artificial image processing after CT imaging, and the use of artificial thresholding can affect the results to some extent. Finally, the need for high resolution also requires the use of small samples, which can be prone to causing secondary cracks during the machining process, leading to deviations in test results [43,47,62]. Table 1 summarizes experimental methods and measurements for testing the pore structure.

Table 1. The experimental methods and measurements for testing the pore structure. Summarized from [43,57–64].

Method	Test Range	Sample Conditions	Advantages	Disadvantages
SEM	>1 nm	Solid rock after conducting treatment	High resolution	No quantitative data
NMR	>4 µm	Standard cylinder rock sample	Indirect observation and display	Not suitable for samples with large porosity
MIP	0.003~400 µm	Core block or core sheet	Quick, wide measuring range	Mercury is toxic,
HPMI	3~500 µm	Core block or core sheet	Applied for open pores, time-saving	damage to core samples, harder to measure the larger pores
Gas adsorption	0.35~50 nm	Rock powder	Good for measuring the small pore size	Narrow measuring range
Micro-CT	>0.5 µm	Standard rock sample	Capable of measuring the close pore	High-cost complex image processing

3. Results and Discussions

Pore structure characterization provides the essential foundation for evaluating reservoir quality, fluid occurrence states, and seepage behavior in carbonate formations. Due to the strong heterogeneity, multiscale pore development, and complex diagenetic modifications of carbonate reservoirs, a single technical approach cannot fully characterize the geometric and topological features of pore systems. This chapter systematically summarizes and discusses representative research findings on carbonate reservoir pore structure characterization, focusing on the following four core aspects: pore-throat structure classification, high-resolution imaging characterization, quantitative petrophysical testing, and pore network modeling and fluid flow implications. By comparing the applicable scales, advantages, and characterization focuses of different methods, this chapter clarifies current understandings of carbonate pore structure characteristics and their controls on petrophysical properties and fluid flow, offering a comprehensive reference for the rational selection and integrated application of characterization techniques.

3.1. Pore-Throat Classification

Gundogar et al. (2016) [11] proposed a pore-throat classification method by correlating mercury intrusion volumes from throats of specific sizes with pore areas derived from SEM image analysis (Figure 2). Based on common inflection points and peak positions in throat-size distributions, four pore-throat classes (PC1 to PC4) were identified, covering pore body sizes of 0.077–310.34 μm and throat diameters of 0.007–23.703 μm (Figure 3). The average coordination number mostly ranged from 3 to 5, and triangular cross-sections dominated the pore system. The pore-to-throat aspect ratio was generally greater than three, indicating a high potential for residual oil saturation during imbibition processes. The porosity and permeability characteristics of the four core samples selected by them in this study (named C013, C016, C019, and C021) are shown in Table 2.

W. Li (2020) classified the pore-throat structure into four types based on the characteristics of the frequency distribution curve of pore-throat radius, wide multimodal, wide bimodal, centralized unimodal, and asymmetric bimodal types and summarized them in Table 3 [108].

They also identified quantitative parameters that are sensitive to four types of pore-throat structures (R_5, S_{kp}, D_r and V_{ma}). R5 represents the pore-throat size where mercury first enters, and this value is positively correlated with reservoir properties. S_{kp} is a measure of the asymmetry of pore-throat sizes frequency distribution curve, representing the relative position of the pore-throat mode. Generally, a good physical property reservoir exhibits coarse skewness, while fine skewness indicates poor physical property. D_r represents the homogeneity of pore-throat sizes—the smaller the value, the more uniform the pore-throat sizes are. V_{ma} refers to the percentage of volume pore-throats larger than 2.5 μm in the whole pore-throat volume. The higher the value, the larger the pore-throats are and the better the reservoir physical properties are.

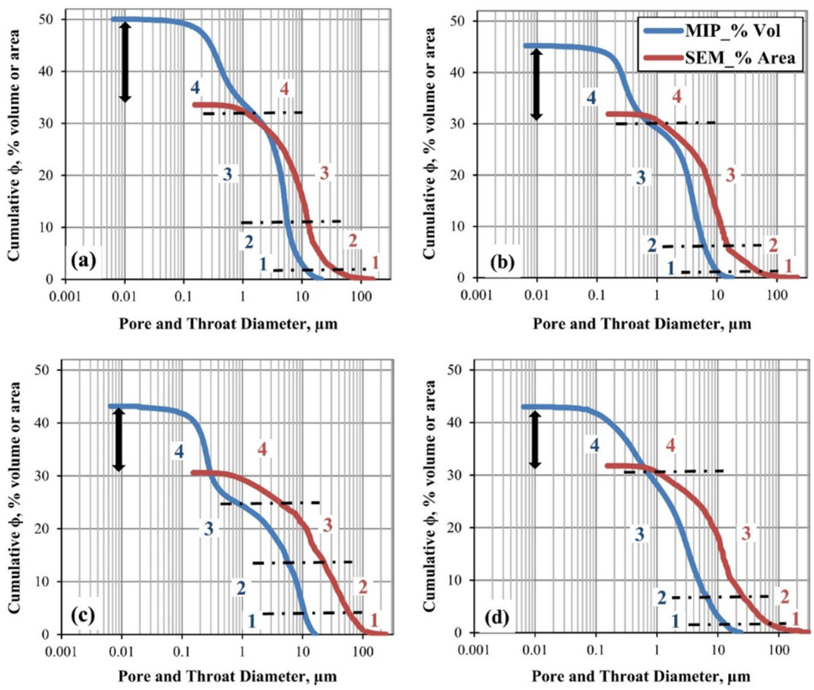

Figure 2. The relationship between MIP throat size and SEM sample area percentage. Adapted from [11].

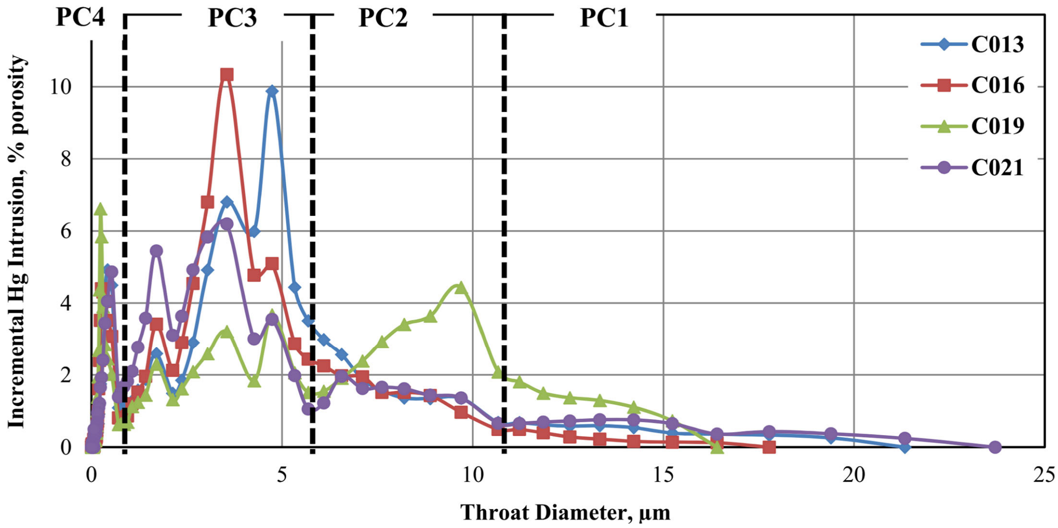

Figure 3. Four throat size ranges and classifications. Adapted from [11].

Table 2. Porosity data from He pycnometry, MIP, and SEM methods as well as core plug porosity and air permeability measurements (sample sizes are widths). Adapted from [11].

Sample	Whole Core Plug (3.81 cm)		Subsamples (0.3–1.2 cm)		
	k_{air} (mD)	$\phi_{meas.}$ (% Volume)	$\phi_{meas.}$ (% Volume) He Pyc.	$\phi_{meas.}$ (% Volume) MIP	SEM ϕ (% Area)
C013	225	51.4	50.0 **52.1** **51.9**	47.2 49.2 50.0	33.6
C016	162	47.7	47.3	45.2	31.9
C019	154	47.0	– **46.5** **46.1**	46.4 44.2 43.2	30.6
C021	212	43.0	48.6	43.0	31.8

Footnote: Columns 2 and 3 represent the air permeability and measured porosity obtained from the whole core plug with a diameter of 3.81 cm. Columns 4 and 5 show the measured porosity from small subsamples (0.3–1.2 cm) tested by helium pycnometry and mercury intrusion porosimetry, respectively. Column 6 denotes the area porosity derived from SEM image analysis. Multiple rows for the same sample correspond to different subsamples or repeated measurements.

The functional relationship between these four sensitive parameters that characterize pore-throat structure and the two principal components F_1 and F_2 is as follows:

$$F_1 = 0.5R_5 - 0.055S_{kp} + 0.663D_r + 0.554V_{ma} \tag{10}$$

$$F_2 = -0.468R_5 + 0.771S_{kp} + 0.06D_r + 0.427V_{ma} \tag{11}$$

The cross plot of F_1 and F_2 (Figure 4) indicates that the pore-throat structure can be well-identified through principal component analysis and quantitative parameters of pore-throat structure.

The expression for the quantitative discrimination index (P) of pore-throat structure is as follows:

$$P = 0.097R_5 + 0.289S_{kp} + 0.412D_r + 0.5V_{ma} \tag{12}$$

The calculation results of the discrimination index P for quantitative identification of four types of pore-throat structures are shown in Table 4.

Table 3. Types of pore-throat structures of Carboniferous KT-I layer in North Truva Oilfield. Adapted from [108].

Pore-Throat Structure Type	Frequency Distribution Curve of Pore-Throat Radii	Average Pore-Throat Radius/μm	Efficiency of Mercury Withdrawal /%	Porosity /%	Permeability /10^{-3} μm
Wide multimodal type	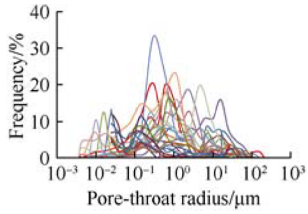	0.30–10.92 (3.42)	16.4–62.5 (39.9)	1.18–25.40 (11.98)	0.07–198.90 (27.90)
Wide bimodal type	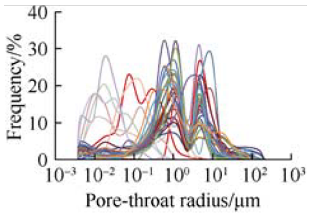	0.03–11.10 (3.52)	6.3–59.1 (33.7)	4.50–35.70 (17.50)	0.01–209.00 (48.70)
Centralized unimodal type	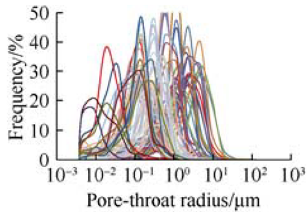	0.01–4.65 (0.90)	2.4–74.1 (33.0)	2.44–38.36 (13.30)	0.01–349.00 (26.70)
Asymmetric bimodal type	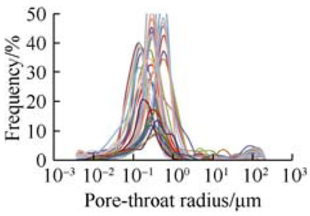	0.25–10.30 (4.10)	8.4–57.7 (27.4)	3.00–16.90 (10.90)	0.01–2.68 (0.56)

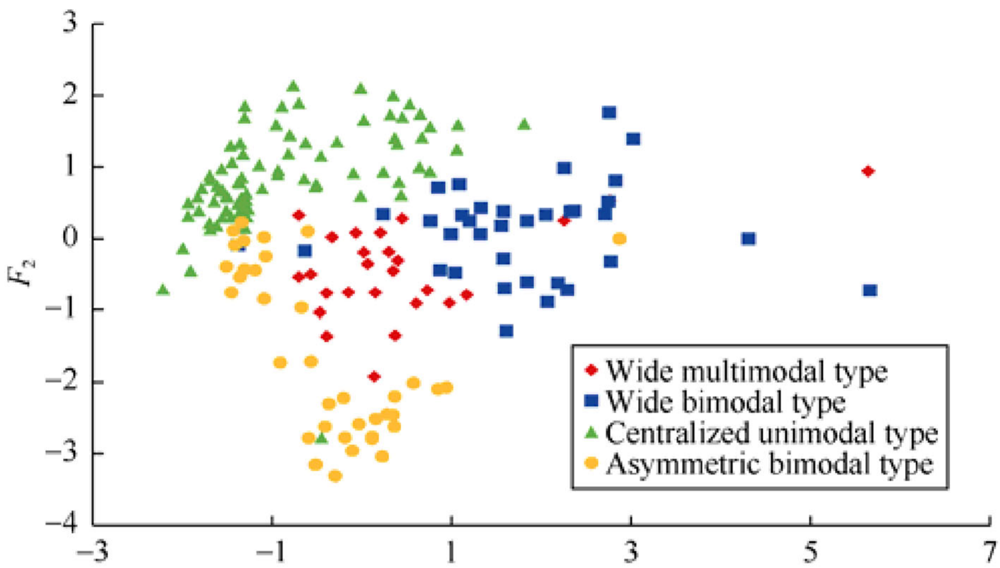

Figure 4. Identification results of different pore-throat structures. Adapted from [108].

Table 4. Quantitative identification criteria for different pore-throat structures. Adapted from [108].

Pore-Throat Structure Type	*P*
Wide multimodal type	0.52–0.77
Wide bimodal type	0.18–0.52
Centralized unimodal type	0.77–1.00
Asymmetric bimodal type	0–0.18

These classification results indicate that carbonate rock pore-throat systems typically exhibit multimodal distribution and strong heterogeneity. The combination of throat size distribution (from mercury intrusion) and pore geometry (from imaging) is more accurate than single method analysis.

3.2. High-Resolution Imaging Characterization of Multiscale Pore Systems

High-resolution imaging techniques visually reveal pore morphology, scale distribution, and spatial configuration, which are indispensable for observing complex carbonate pore structures.

3.2.1. SEM-Based Two-Dimensional Pore Characterization

Wang et al. (2012) [44] performed a study on multi-scale characterization of pore structure in carbonate formations. They discovered that the lower resolution images displayed macropore properties, while the higher resolution images showed micropore properties when observing SEM images of thin section carbonate. Figure 5 shows the imaging of carbonate thin sections with resolutions of 1.34 µm (Figure 5a) and 0.335 µm (Figure 5b) using scanning electron microscopy.

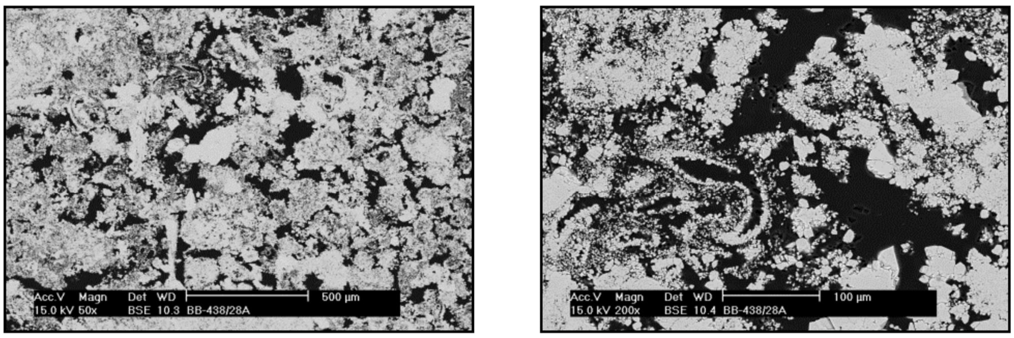

(a) Low resolution image (b) High resolution image

Figure 5. SEM images of 1.34 µm and 0.335 µm resolutions. Adapted from [44].

They used a Markov Chain Monte Carlo (MCMC) method to construct 3D macropore and micropore digital rocks respectively and then applied superposition method to construct multiscale digital rocks based on the macropore and micropore. The resultant 3D digital rocks had a volume of 100^3 to 400^3 voxels. The porosity of macropore digital rock (Figure 6a) is 0.2544, with a resolution of 1.34 µm; the porosity of micropore digital rock (Figure 6b) is 0.3546, with a resolution of 0.335 µm. Overlay micro digital core and macro digital core to observe pores characteristics, as shown in Figure 6c. The porosity of stacked digital rock is 0.5189, with a resolution of 0.335 µm. It is worth noting that 3D reconstruction based on 2D data and MCMC modeling is model-based, and the results depend on the assumptions made and may not fully reflect the actual pore structure.

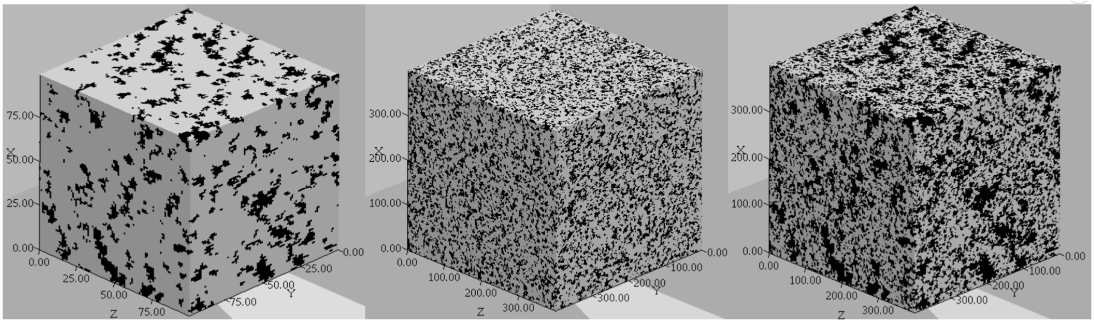

(a) Macro pore digital rock (b) Micro pore digital rock (c) Superposition digital rock

Figure 6. Different digital rocks. Adapted from [44].

They used pore analysis tools to perform flow rate calculations on the extracted network models from macropore, micropore and superposition pore, respectively. It can be clearly seen from Figure 7 that the curve of the superposition network is sandwiched between the macropore network curve and the micropore network curve, indicating that the superposition network has the geometric and topological characteristics of macroscopic pore network and microporous network.

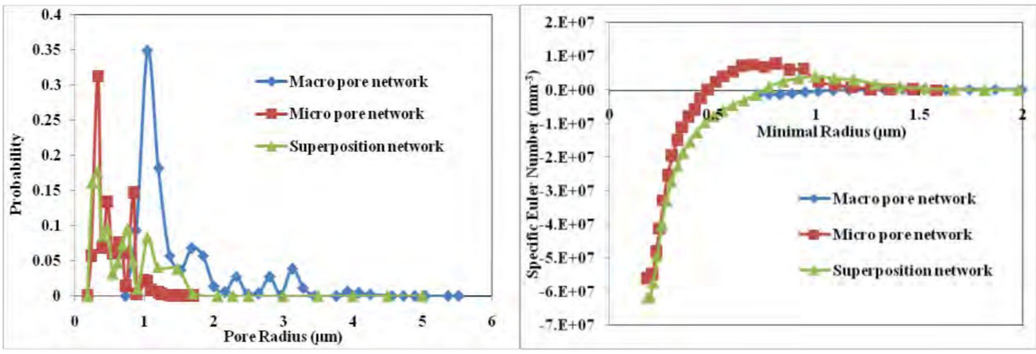

Figure 7. Geometry and topology parameters comparison of pore network models. Adapted from [44].

Duan et al. (2018) [109] conducted a study on the pore structure of carbonate rocks using SEM technology and identified four typical nano-/microporous types (Figure 8).

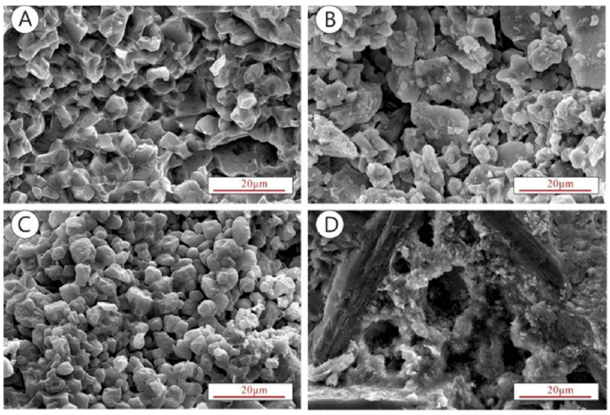

Figure 8. Four nano-/micropore types under the SEM. (**A**) Pores between fully coalescent polyhedral to anhedral crystals; (**B**) pores between the elongate scaleno-rhombohedral crystals; (**C**) pores between the rounded anhedral to subhedral micrite crystals; (**D**) pores between the dissolved euhedral to subhedral dolomite crystals. Adapted from [109].

The researchers conducted a study on the poresystem of saline-lacustrine tight oil carbonate reservoir using scanning electron microscopy (SEM) [110]. They found that reservoir pore system is mainly composed of microfractures (Figure 9a,e), dissolution pores (Figure 9b–e) and intercrystalline pores (Figure 9c–f). It is concluded that content of dolomite is associated with a larger number of intercrystalline pores and, consequently, higher porosity of reservoir. It can be seen that the pore is developed at multiscale from nanometer, micrometer to macroscopic. The observation that natural fractures (especially open fractures) dominate permeability and productivity, and are the main channels for fluid migration, confirms the findings of Belfield et al. in 1988 [111].

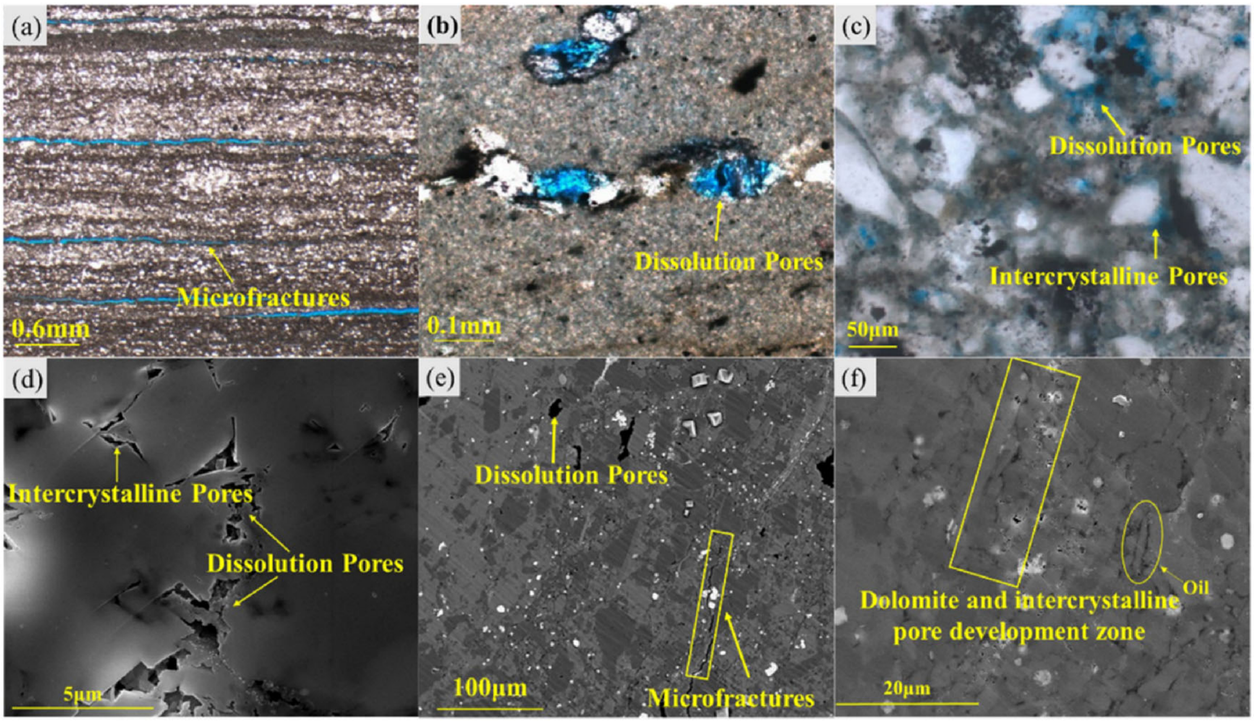

Figure 9. Pore system obtained by thin section and SEM. (**a**) A couple of parallel microfractures; (**b**) secondary enlarged pores created by chemical action; (**c**,**d**) dissolution pores and intercrystalline pores created by dolomitization; (**e**) dissolution pores and microfractures; (**f**) oil reserved in intercrystalline pores and microfractures. Adapted from [110].

3.2.2. X-Ray CT-Based Three-Dimensional Pore Characterization

Huang et al. (2016) [112] constructed a 3D pore network model for a carbonate reservoir using data from X-ray computed tomography (CT) scans. They found that the pore structure of the carbonate reservoir is heterogeneous, with varying pore sizes, shapes, and connectivity. The pore network model was used to simulate fluid flow in the reservoir, and the results showed that the fluid flow is highly influenced by the pore structure.

Zhang et al. (2022) [113] proposed a new method for evaluating differences in rock pore structure. They developed a hybrid pore network model that combines the advantages of both geometric and flow-based pore network models to better capture the complex pore structure of carbonate rocks. The model was validated using X-ray computed tomography (CT) data and was used to simulate fluid flow in carbonate rocks. The results showed that the hybrid model was more accurate than either of the individual models in predicting fluid flow. Y. Zhang (2019) [114] compared the structural characteristics of different rock types, including five carbonate rocks and two limestone samples (Figure 10). The information of seven rock samples is shown in Table 5, and the micro-CT images of these samples were provided by Imperial College London.

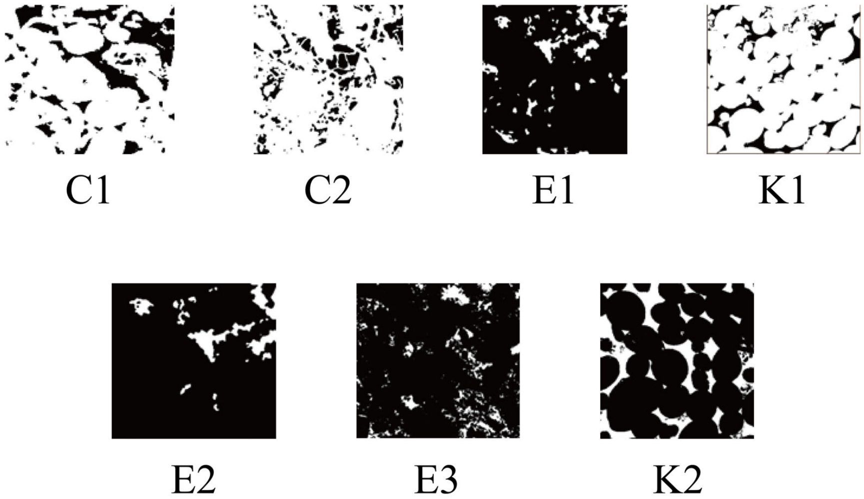

Figure 10. 2D cross section of micro-CT images samples used in the study. Adapted from [114].

Table 5. Image information of the studied rock samples. Adapted from [114].

Samples	Pixel (μm)	Size (Pixel^3)	Rock Type	Porosity (%)
C1	2.85	300 × 300 × 300	carbonate	23.3
C2	5.345	300 × 300 × 300	carbonate	16.8
KC	3.00006	1024 × 1024 × 1024	carbonate	---
KL	2.645	1024 × 1024 × 1024	limestone	---
E1	3.31136	650 × 650 × 650	carbonate	---
E2	3.31136	500 × 500 × 500	carbonate	---
EL	2.6825	1024 × 1024 × 1024	limestone	---

In the present study, 3D digital core samples were reconstructed, and porosity was derived by quantifying the number of voxels in the images. On this basis, the relationships of connected porosity and total porosity with sample size were analyzed.

Figure 11 presents the porosity–size relationship curves for all seven samples in a single multi–panel plot. As seen in Figure 11a–e, the total porosity and connected porosity of carbonate samples are noticeably affected by sample size. Most pores in C1, C2, and KC are well-connected, whereas E1 and E2 contain a large number of isolated pores. For the limestone samples shown in Figure 11f,g, sample size has only a weak effect on EL, while KL shows a strong size dependence with nearly all pores being connected.

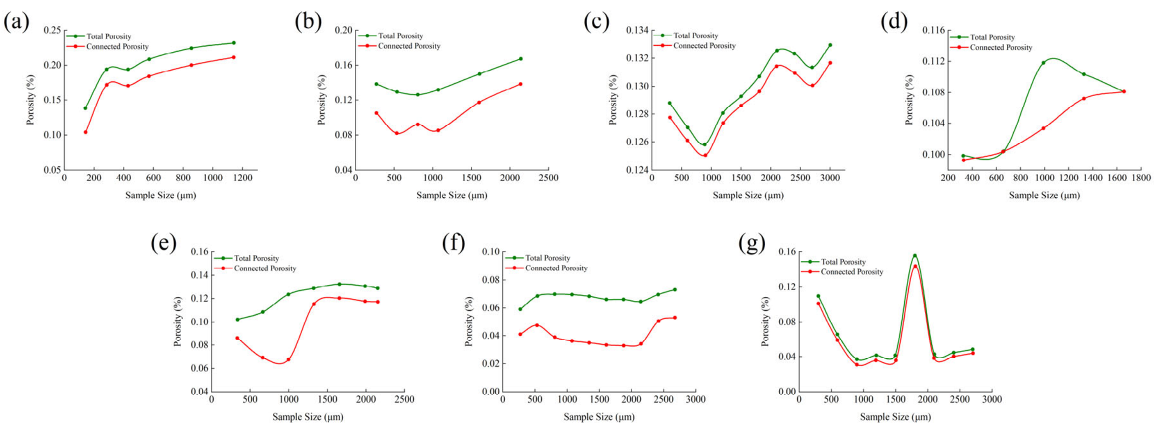

Figure 11. Porosity–size relationship curves for all seven samples. (**a**) C1, (**b**) C2, (**c**) KC, (**d**) E1, (**e**) E2, (**f**) EL, (**g**) KL. Adapted from [114].

CT scanning enables the identification of both connected and isolated pores, differentiation between fractures and pore networks, quantification of mean pore and throat dimensions, comparative analysis of pore-throat architectures across various lithologies, simulation of fluid flow within the pore space, and full three-dimensional visualization of rock-sample characteristics. Al-Kharusi and Blunt (2007) [115] completed a study on two carbonate rock samples. They analyzed the carbonate core plug of Oman Petroleum Development Company. A thin section was cut from the core plug and imaged at various resolutions using scanning electron microscopy (Figure 12).

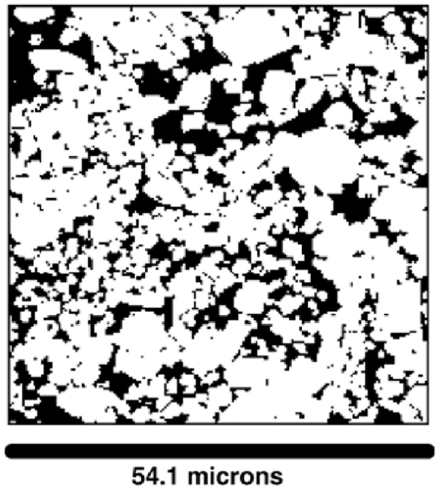

Figure 12. 2D SEM image of the carbonate sample, from which the 3D network was extracted (black areas denote pore spaces). Adapted from [115].

The image at this stage is a 2D image. For this carbonate, the pore space could not be readily resolved using micro-CT scanning. Okabe and Blunt (2004) then fed the digitized 2D image into the algorithm developed [116], which uses multiple-point statistics to generate a 3D digital image that reproduces the patterns observed in the 2D slice. By using network extraction algorithm to process 3D images, a topologically representative network of the carbonate rock can be obtained. The carbonate network consists of 643 pores and 2623 throats. The network is shown in Figure 13.

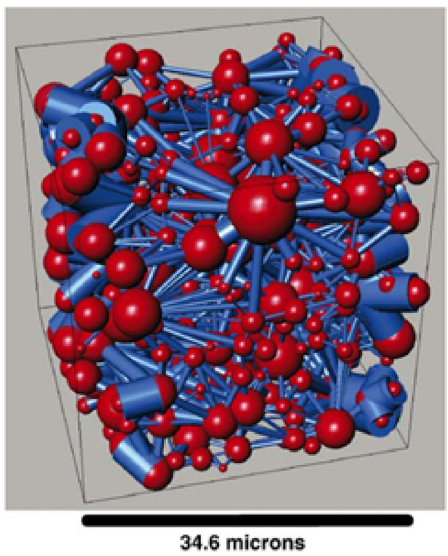

Figure 13. Three-dimensional image of the extracted pore network for the carbonate sample (1283 voxels). Adapted from [116].

Wang et al. (2020) integrated high-pressure mercury injection capillary pressure curves with petrophysical and petrographic data to classify the ultradeep (>4950 m) carbonate gas-reservoir samples from the Deng IV Member, Sichuan Basin, into the following four distinct reservoir types: (1) matrix, (2) pore, (3) cavity, and (4) fracture-cavity [117]. Perform two resolution (13.15 μm and 0.98 μm) CT scans on typical core samples of four types, obtaining over 8000 two-dimensional slice images. Based on the 13.15 μm resolution image, three types of reservoir spaces, fractures, cavities and large pores can be observed (Figure 14a,c,e,g). At a resolution of 0.98 μm, only pores of different sizes and rock matrixes can be observed (Figure 14b,d,f,h). They also used the "maximum ball algorithm" based on CT images to extract pores and throats, constructed a 3D "ball-stick" network model (Figure 15), and quantified parameters such as radius (Figure 16), volume, and coordination number of pores and throats. Based on the 13.15 μm resolution, the pore-throat coordination numbers for the matrix type, pore type, cavity type and fracture-cavity type samples are 2.81, 3.59, 3.37 and 5.46, respectively (Figure 17). For the 0.98 μm resolution, the pore-throat coordination numbers for the matrix type, pore type, cavity type and fracture-cavity type samples are 2.44, 4.13, 4.51 and 4.79, respectively (Figure 18).

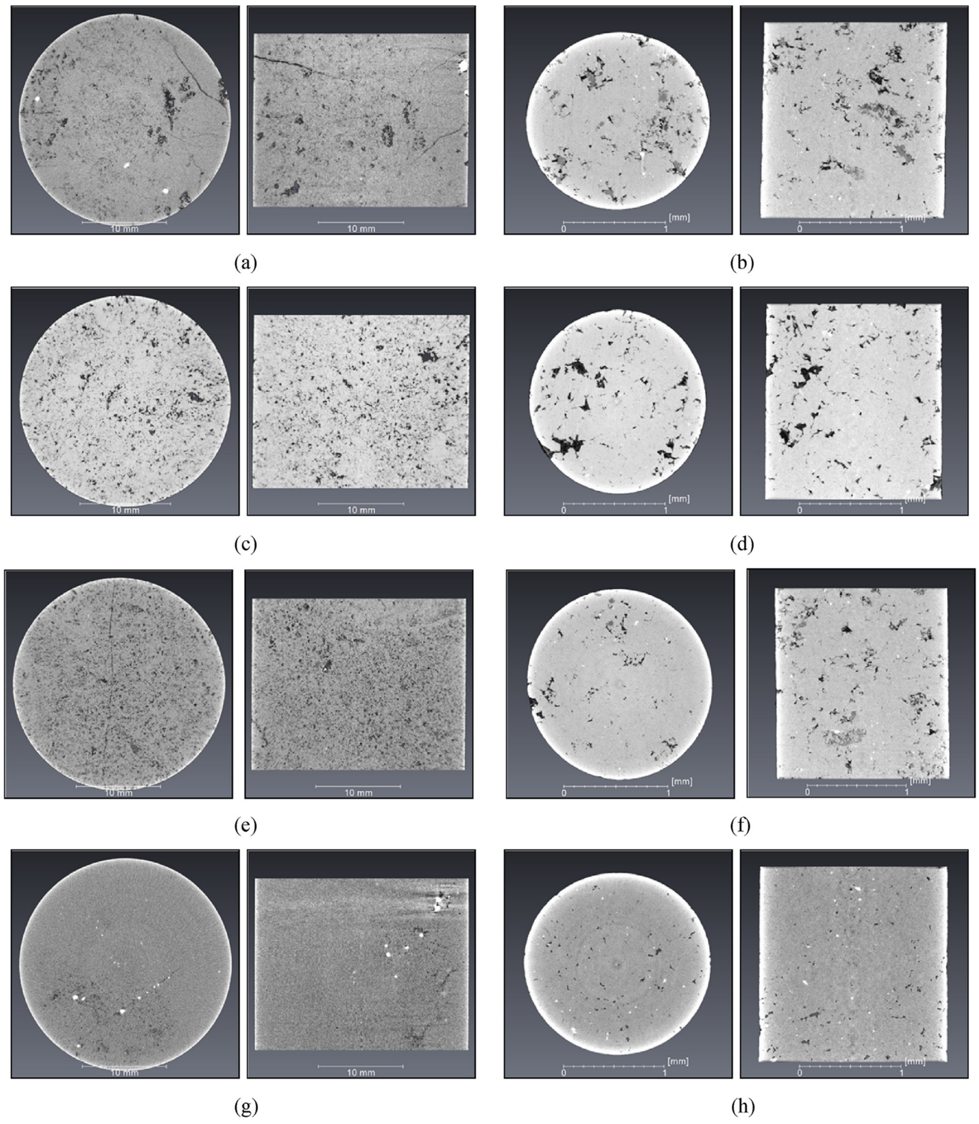

Figure 14. CT scanning images of multitype core at resolutions of 13.15 μm (left column) and 0.98 μm (right column): (**a**,**b**) fracture-cavity type; (**c**,**d**) cavity type; (**e**,**f**) pore type; (**g**,**h**) matrix type. Adapted from [117].

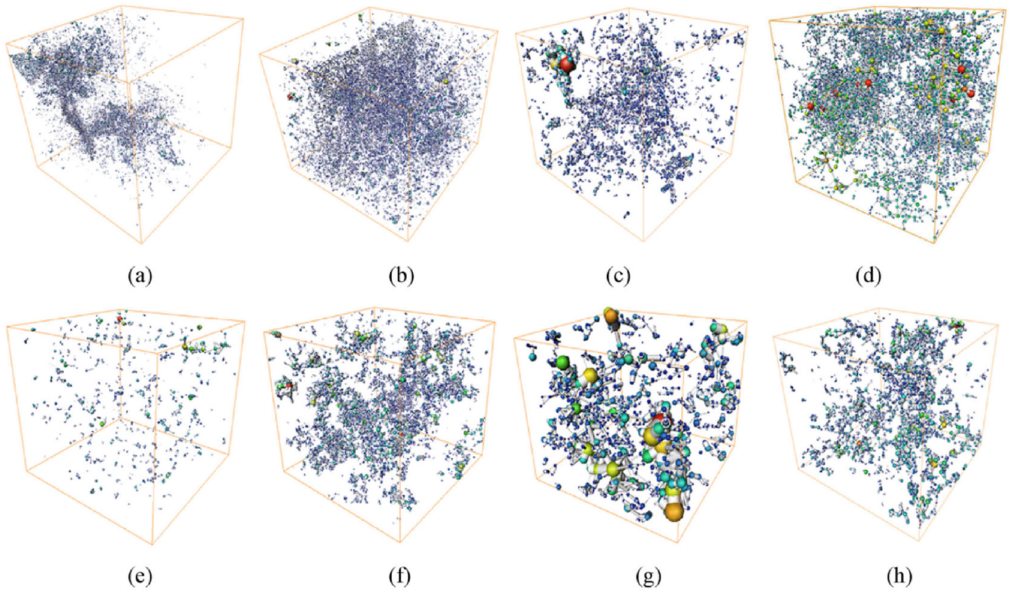

Figure 15. Pore-throat connectivity and network topological structures at resolutions of 13.15 μm (first row) and 0.98 μm (second row): (**a**,**e**) matrix type; (**b**,**f**) pore type; (**c**,**g**) cavity type; (**d**,**h**) fracture-cavity type. Adapted from [117].

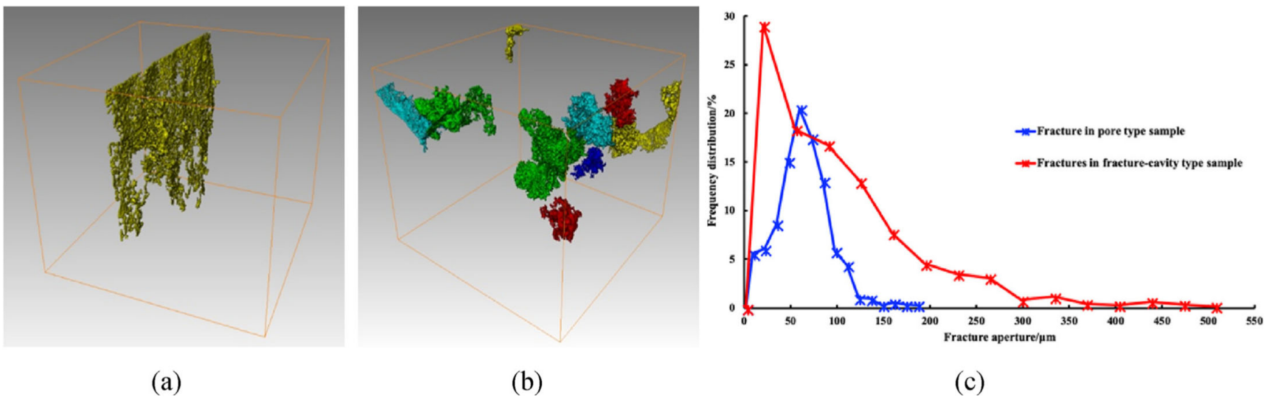

Figure 16. Fracture network topology and aperture distribution: (**a**) one fracture in pore type sample; (**b**) ten fractures in fracture-cavity type sample; (**c**) fracture aperture distribution. Adapted from [117].

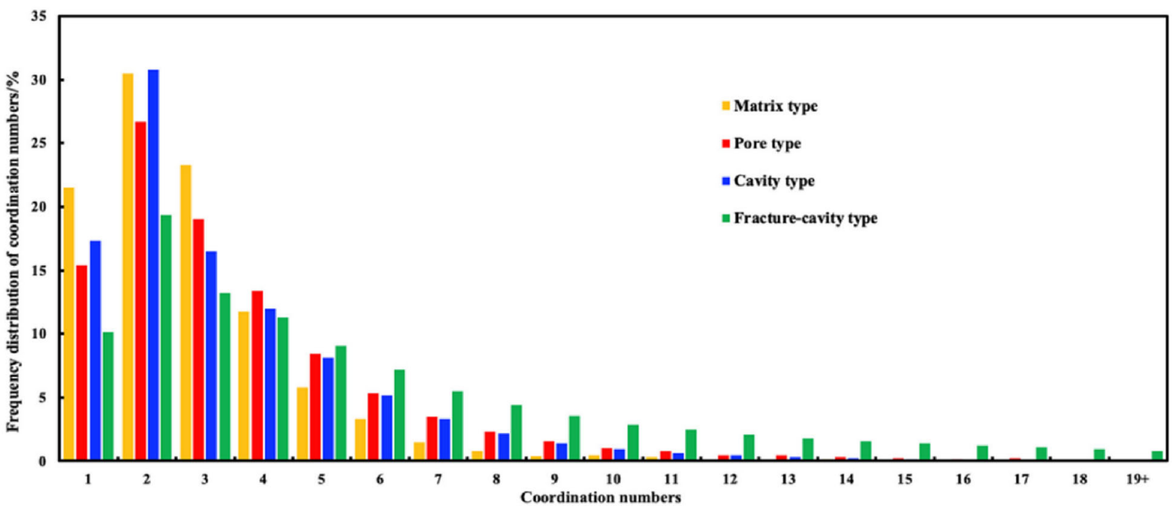

Figure 17. The coordination numbers from four types of samples at resolutions of 13.15 μm. Adapted from [117].

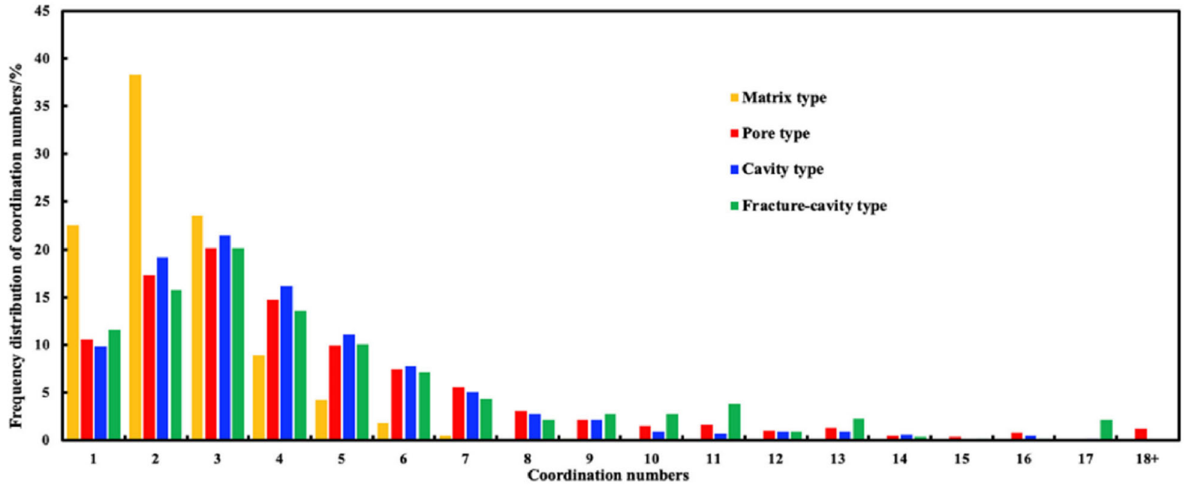

Figure 18. The coordination numbers from four types of samples at resolutions of 0.98 μm. Adapted from [117].

Wang et al. (2020) performed micro-nano-CT scan on core samples B′ and E′ for and extracted a 45 mm^3 cube from the 3D pore network model shown in Figure 19C to observe pore–throat distributions (Figure 20) [118]. The results show that the porosity of the 3D digital core B′ is 2.51%, whereas that of core E′ is 2.64%. The corresponding laboratory-measured porosities are 2.43% and 2.60%, respectively. Research results show that micropore absence does not impact the network connectivity of digital rock cores.

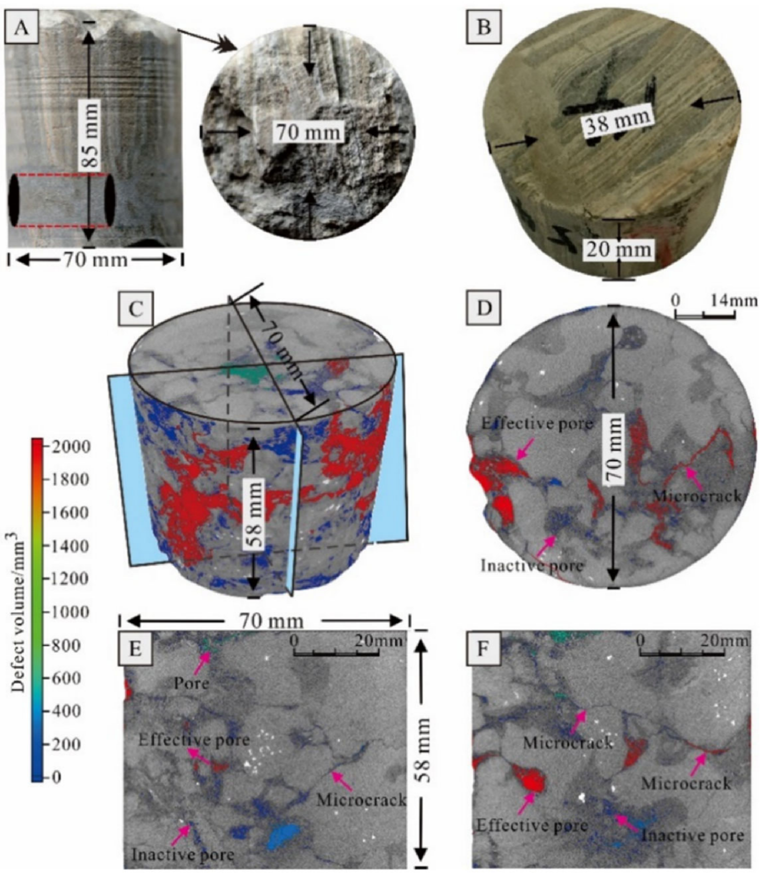

Figure 19. Pore and fracture features of mixed carbonate rocks. (**A**) Crude core; (**B**) acidified core; (**C**) CT scanning image; (**D**) top slice of core; (**E**) right slice of core; (**F**) front slice of core. Adapted from [118].

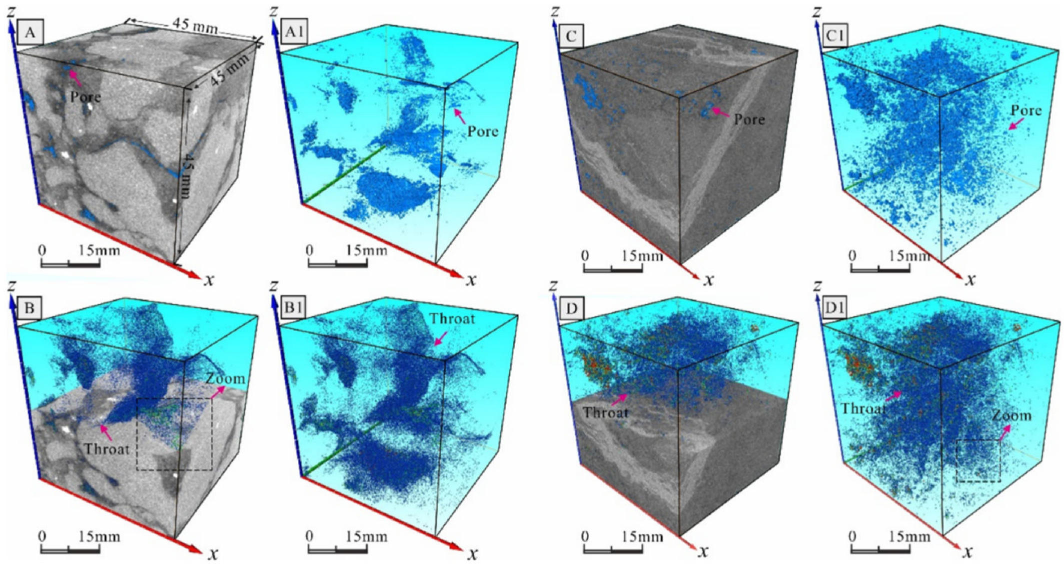

Figure 20. CT images of pore-throat radius distribution in samples. (**A**) The pore of B′; (**B**) the throat of B′; (**C**) the pore of E′; (**D**) the throat of E′. Adapted from [118].

3.3. Quantitative Petrophysical Characterization of Pore Structure

As a core testing method, rock physics experiments can systematically provide quantitative data on key parameters such as pore size distribution, porosity, throat connectivity, and specific surface area. These basic data can accurately characterize the intrinsic characteristics of rock pore systems and provide a real theoretical basis for the quantitative characterization of rock pore structure.

3.3.1. Mercury Injection Capillary Pressure (MICP)

Mercury injection capillary pressure is widely used to measure throat-size distribution and capillary pressure. High-pressure mercury intrusion (HPMI) effectively characterizes throats in the range of 3–500 μm and supports rapid classification of pore and reservoir types. However, high injection pressure may compact small pores, reducing accuracy, and it is less suitable for nanoscale pores (<50 nm) in tight reservoirs. MIP only measures interconnected (effective) porosity and cannot detect isolated pores.

3.3.2. Nuclear Magnetic Resonance (NMR)

Genty et al. (2007) [119] developed a quantitative method for characterizing carbonate reservoir pore structures and identifying genetic pore types based on nuclear magnetic resonance (NMR) T_2 spectra. The $\log(T_2)$ distribution of NMR signals was decomposed into up to three Gaussian components, yielding nine basic parameters including component weights, means, and standard deviations. The following two geologically significant quantitative parameters were then extracted: μ_{max}, defined as the largest mean pore size among components with weight proportion greater than 0.1, and σ_{main}, representing the standard deviation of the dominant pore component, as illustrated in Figure 21. These two parameters quantitatively describe the maximum average pore size and the homogeneity of the dominant pore size, respectively. A Bayesian classification model was further established to realize quantitative identification of the following six genetic pore types: matrix, cemented, intergranular, dissolution-enhanced, intercrystalline, and vuggy pores. Verified by 103 core samples, the prediction accuracy ranges from 60% to 90%. This method enables rapid quantitative evaluation of pore structures using NMR logging in uncored or poorly cored intervals, providing a reliable tool for detailed characterization and distribution prediction of complex carbonate reservoirs.

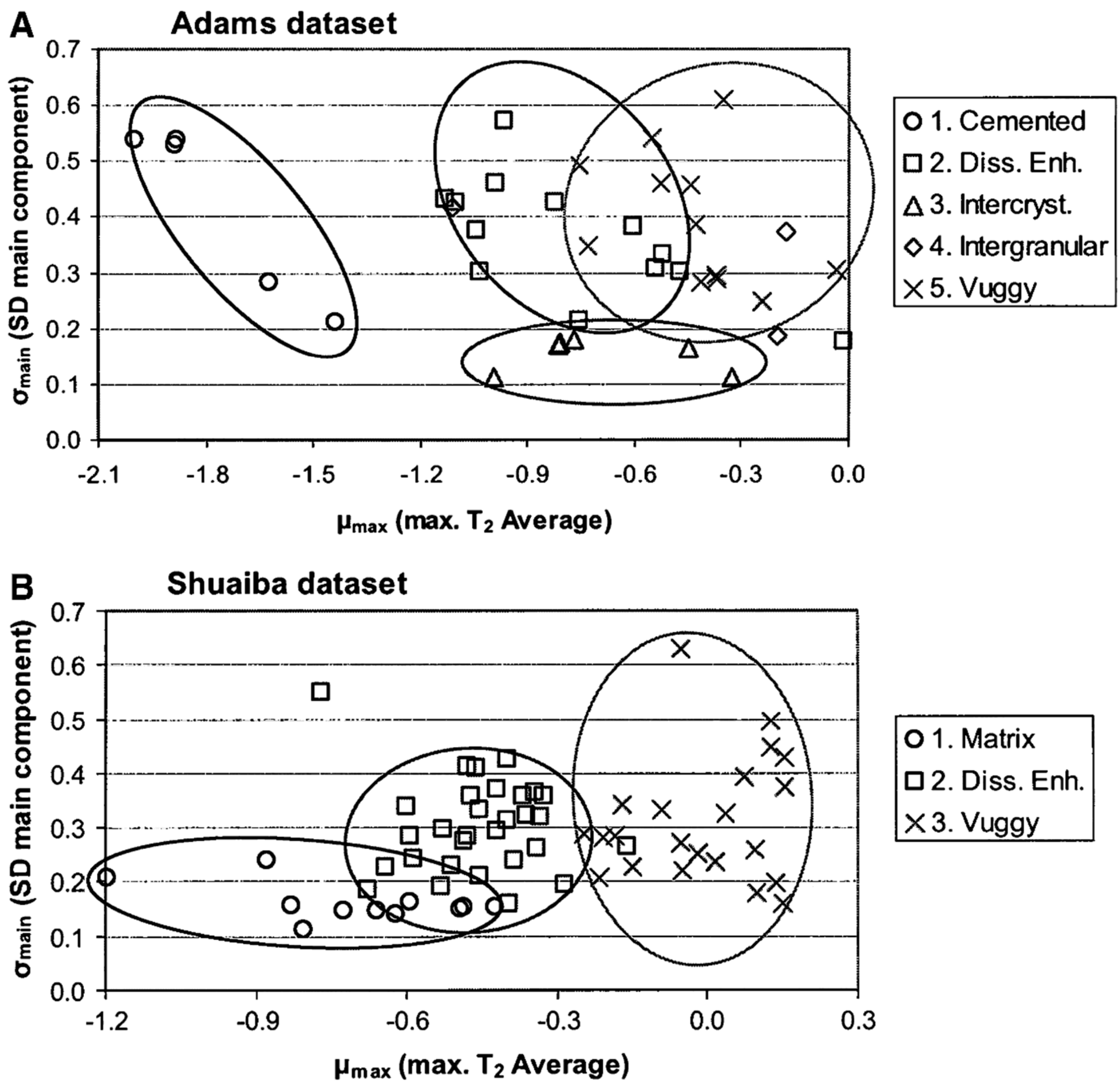

Figure 21. Bivariate plot of two key parameters μ_{max} vs. σ_{main}: (**A**), Adams data set; (**B**), Shuaiba data set. Adapted from [119].

3.3.3. Gas Adsorption and Other Methods

Gas adsorption (N_2, CO_2) is suitable for measuring nanopores (0.35–50 nm) and yields specific surface area and pore-size distribution. It is cost-effective and reliable for micropore analysis but has a narrow measurement range and is unsuitable for large or complex pores. Helium pycnometry provides highly accurate matrix volume and total porosity, serving as a benchmark for calibrating other methods.

3.3.4. The Comparison and Connection Between Different Characterization Techniques

MICP technology is widely used for measuring throat size distribution and capillary pressure due to its simple operation and intuitive results. NMR technology also has the characteristics of fast and non-destructive measurement. Tian et al. (2018) [120] quantitatively characterized pore structures in ultra-deep tight carbonate reservoirs in the Tahe Oilfield, China. They used MICP to analyze pore-throat size, connectivity and type, and NMR to determine pore size distribution and pore compressibility. They compared the test results of six rock types, as shown in Figure 22.

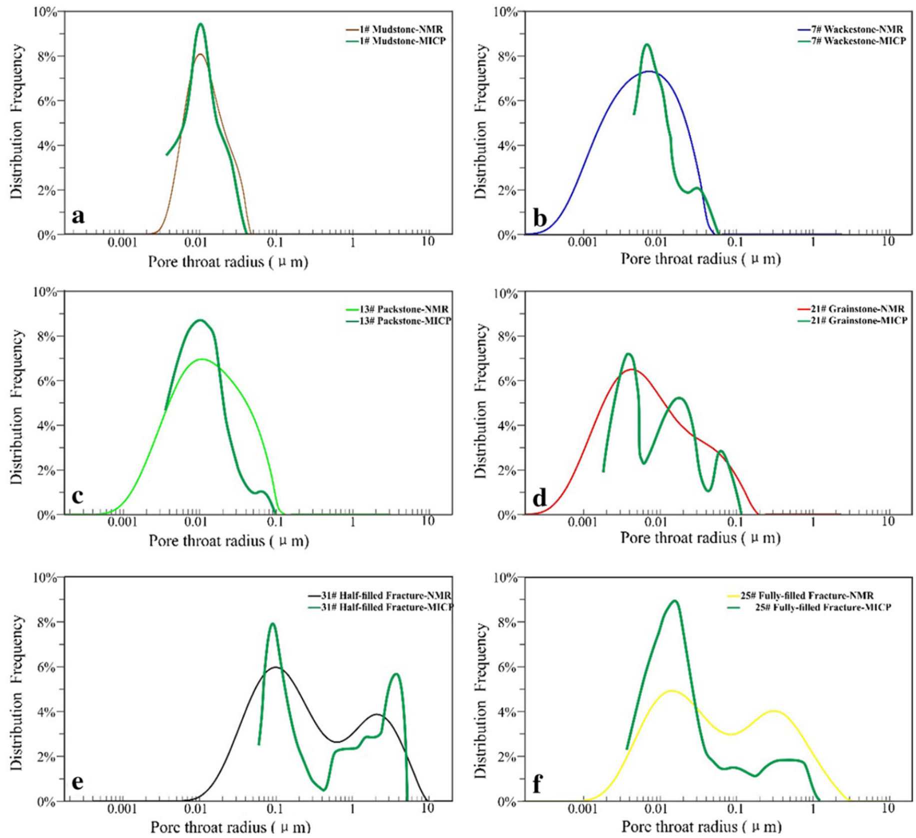

Figure 22. The pore structure distributions from the MICP and NMR experiments for the six rock types. (**a**) Mudstone, (**b**) wackestone, (**c**) packstone, (**d**) grainstone, (**e**) limestone with half-filled fractures, (**f**) limestone with fully filled fractures. Adapted from [120].

The comparison between MICP and NMR pore structure distributions demonstrates that the two methods yield consistent overall trends in pore size characterization. Minor differences arise because MICP reflects connected pore throats while NMR measures total water-saturated pore space, and their agreement is significantly improved by rock-type classification. This confirms that NMR can serve as a rapid, nondestructive alternative to MICP for pore structure evaluation in tight carbonates.

3.4. Implications for Fluid Flow

The pore structure characterization of carbonate formations has important implications for understanding fluid flow in porous media. The reviewed studies have shown that the pore structure of carbonate formations is complex and diverse, with various pore types and sizes. This complexity can impact fluid flow behavior in several ways.

So, the pore structure of carbonate formations is complex and diverse, and multiple methods and scales must be used to fully characterize it. Pore-throat classification, imaging techniques such as X-ray computed tomography (CT) and scanning electron microscopy (SEM), and pore network modeling are effective methods for pore structure characterization. These methods provide valuable insights into the pore structure of carbonate formations and can aid in the understanding of fluid flow in porous media, which is important for oil and gas production and groundwater management.

First, the pore-throat classification method developed by Gundogar et al. (2016) [11] identified four pore-throat classes with unique pore- and throat-size distributions. The pore-to-throat aspect ratio was generally large, indicating the potential for significant residual oil saturation. This information can help in understanding the flow behavior of oil and gas in carbonate formations.

Second, the imaging techniques used by Wang et al. (2012) [118], Duan et al. (2018) [109], and Wang et al. (2018) [5] revealed that the pore size distribution of carbonate formations is mainly in the range of 0.1–10 μm, with irregular pore shapes and poor pore connectivity. These characteristics can affect fluid flow behavior by limiting the flow of fluids through the pore network, creating regions of stagnant fluid, and affecting the capillary pressure and wettability of the rock.

Furthermore, the quantitative analysis of the 3D pore-throat network topology used by Wang et al. (2020) [117] showed that the fracture-cavity type reservoirs possess the highest coordination number, multiple flow paths, and minimal seepage resistance; the cavity-type reservoirs are mainly characterized by large pore throats, which help reduce seepage resistance and belong to buffer zones for fluid flow; the pore-type reservoirs possess moderate coordination numbers, mainly characterized by necking and lamellar throats, and moderate seepage resistance; the matrix-type reservoir possesses the lowest coordination number, the strongest seepage resistance, and only local weak flow exists. Furthermore, they also found that a single pore or throat is insufficient to enable efficient fluid flow, and the coordinated development of fractures and cavities greatly improves the reservoir permeability.

The flow patterns of oil and gas in different reservoir spaces within carbonate rocks vary greatly. If the fracture and cavity are connected, the oil and gas inside the connected cavity will quickly flow towards the fracture under the drive of pressure difference; if it is an isolated cavity, when the fluid in the main fracture first flows towards the wellbore to form a pressure drop, the oil and gas in the isolated cavity are supplied to the main fracture through "microcrack flow" or "matrix infiltration"; the flow mode in the cavity is dominated by gravity inertia free surface flow, where the oil phase first spreads along the bottom of the cavity and then the water phase sinks from the top of the cavity, ultimately forming attic residual oil. In the flow mode of pores, slippage, diffusion, and imbibition are the main modes, the oil phase transforms from "oil film on rock wall " to "isolated oil droplets" and is gradually imbibed and peeled off by the water phase (Figure 23).

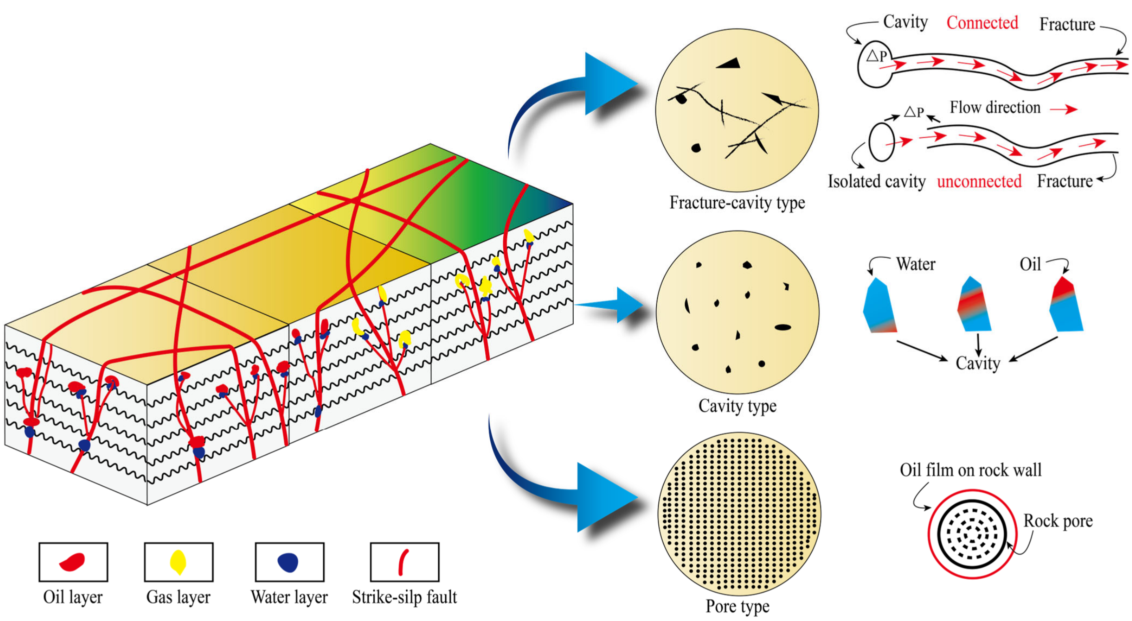

Figure 23. Oil and gas flow patterns in different reservoir spaces of carbonate rocks. Adapted from [117].

The reviewed studies highlight the importance of fully characterizing the pore structure of carbonate formations to understand fluid flow behavior. The results have important implications for the development of effective extraction methods for oil and gas reservoirs and can contribute to a better understanding of groundwater flow in aquifers and geologic formations.

4. Future and Challenges

Current pore structure characterization methods still face several practical limitations. Imaging techniques such as SEM and micro-CT are restricted by resolution and observable scale, making it difficult to capture multiscale pore systems simultaneously. Most testing methods are limited to specific pore size ranges, and few can achieve full-scale coverage from nanometers to millimeters. High testing costs, complex sample preparation, and destructive testing also reduce efficiency in practical applications. In addition, digital rock reconstruction and pore network modeling rely heavily on model assumptions, which may not fully reflect the true heterogeneity of carbonate rocks.

In recent years, machine learning (ML) has also been increasingly used in pore structure characterization. For example, ML-based intelligent image segmentation can effectively improve the efficiency and accuracy of pore extraction from SEM and CT images, reducing the uncertainty caused by manual processing. Data-driven ML models also provide reliable predictions for petrophysical parameters such as permeability and pore size distribution. These methods do not need to become the core of this review, but they represent an important development direction for efficient and automated pore analysis.

Future research should focus on developing high-precision, low-cost multiscale imaging techniques that can integrate multiple methods efficiently. More robust and generalized pore network models are needed to reduce dependence on manual processing and model assumptions. It is also necessary to establish standardized workflows for multiscale characterization, so that pore structure parameters can be more reliably applied to reservoir evaluation and fluid flow prediction.

5. Conclusions

This paper reviews typical methods used to characterize pore structures in carbonate oil and gas formations, such as SEM, NMR, MIP, micro-CT, and pore network modeling. Carbonate reservoirs are highly heterogeneous and contain complex diagenetic pores with a wide range of sizes, so they must be tested using multiple methods across different scales.

SEM clearly shows pore morphology, diagenetic structures, and secondary pores at micro- and nanoscales, and can support quantitative analysis through image processing. NMR uses T_2 relaxation signals to indirectly measure pore size distribution and connectivity and works well in carbonates with weak magnetic interference. MIP and HPMI quickly quantify pore-throat size distributions but cannot reliably measure nanoscale pores and may damage samples. Micro-CT provides non-destructive 3D imaging of connected and isolated pores, but it is limited by resolution, cost, and sample representativeness. Pore network modeling helps quantify structural heterogeneity and its influence on fluid flow.

Current methods still face several key limitations. These include mismatched scales among different techniques, insufficient quantitative accuracy, model dependence in digital reconstruction, and high costs for multi-scale testing. These problems make it difficult to accurately evaluate pore connectivity and flow characteristics in complex carbonates.

This review integrates a variety of characterization methods and clarifies their applicability, advantages, and limitations in carbonate formations. It provides practical guidance for method selection in reservoir evaluation. Future research should develop high-precision multi-scale imaging, intelligent image segmentation, and more universal pore network models. These improvements will support efficient, low-cost, and full-scale pore structure characterization for carbonate reservoirs.

Funding: The authors sincerely this research was funded by the Anhui Provincial Key Research and Development Programs (grant number 2022n07020003), the Anhui Provincial Natural Science Foundation (grant number 1908085MD105), the China Postdoctoral Science Foundation (grant number 2019M662200), and the Outstanding Innovative Research Team in Higher Education Institutions of Anhui Province (grant number 2022AH010081). This work was also supported by the Scientific Research Foundation for High-level Talents, China University of Geosciences (grant number 102-162301212673). The APC was funded by China University of Geosciences.

Data Availability Statement: No new data were created or analyzed in this study.

Conflicts of Interest: The authors declare no competing financial interests.

References

1. Garing, C.; Luquot, L.; Pezard, P.A.; Gouze, P. Electrical and Flow Properties of Highly Heterogeneous Carbonate Rocks. *AAPG Bull.* **2014**, *98*, 49–66. [CrossRef]
2. Kolawole, O.; Millikan, C.; Kumar, M.; Ispas, I.; Schwartz, B.; Weber, J.; Badurina, L.; Šegvić, B. Impact of Microbial-Rock-CO_2 Interactions on Containment and Storage Security of Supercritical CO_2 in Carbonates. *Int. J. Greenh. Gas. Control* **2022**, *120*, 103755. [CrossRef]
3. Luo, Q.; Zhang, C.; Dai, Q.; Liu, D.; Yang, W.; Liu, L.; Kong, X.; Wang, X.; Liu, X.; Yang, K. Characterization of Compact Carbonate Pore–Throat Network Systems in the Xiagou Formation in Qingxi Sag, Jiuquan Basin, China. *J. Pet. Sci. Eng.* **2017**, *159*, 853–868. [CrossRef]
4. Tiab, D.; Donaldson, E.C. Naturally Fractured Reservoirs. In *Petrophysics*; Elsevier: Amsterdam, The Netherlands, 2016; pp. 415–481. ISBN 978-0-12-803188-9.
5. Wang, L.; Yang, S.; Peng, X.; Deng, H.; Meng, Z.; Qian, K.; Wang, Z.; Lei, H. An Improved Visual Investigation on Gas–Water Flow Characteristics and Trapped Gas Formation Mechanism of Fracture–Cavity Carbonate Gas Reservoir. *J. Nat. Gas. Sci. Eng.* **2018**, *49*, 213–226. [CrossRef]
6. Zhang, K.; Pang, X.; Zhao, Z.; Shao, X.; Zhang, X.; Li, W.; Wang, K. Pore Structure and Fractal Analysis of Lower Carboniferous Carbonate Reservoirs in the Marsel Area, Chu-Sarysu Basin. *Mar. Pet. Geol.* **2018**, *93*, 451–467. [CrossRef]
7. Amour, F.; Mutti, M.; Christ, N.; Immenhauser, A.; Agar, S.M.; Benson, G.S.; Tomás, S.; Alway, R.; Kabiri, L. Capturing and Modelling Metre-Scale Spatial Facies Heterogeneity in a Jurassic Ramp Setting (Central High Atlas, Morocco). *Sedimentology* **2012**, *59*, 1158–1189. [CrossRef]
8. Hosa, A.; Wood, R. Quantifying the Impact of Early Calcite Cementation on the Reservoir Quality of Carbonate Rocks: A 3D Process-Based Model. *Adv. Water Resour.* **2017**, *104*, 89–104. [CrossRef]
9. Lucia, F.J. Petrophysical Parameters Estimated from Visual Descriptions of Carbonate Rocks: A Field Classification of Carbonate Pore Space. *J. Pet. Technol.* **1983**, *35*, 629–637. [CrossRef]
10. Van der Land, C.; Wood, R.; Wu, K.; van Dijke, M.I.J.; Jiang, Z.; Corbett, P.W.M.; Couples, G. Modelling the Permeability Evolution of Carbonate Rocks. *Mar. Pet. Geol.* **2013**, *48*, 1–7. [CrossRef]
11. Gundogar, A.S.; Ross, C.M.; Akin, S.; Kovscek, A.R. Multiscale Pore Structure Characterization of Middle East Carbonates. *J. Pet. Sci. Eng.* **2016**, *146*, 570–583. [CrossRef]
12. Milad, I.B.; Farmer, R.; Saidian, M. Permeability Prediction in a Complex Carbonate Reservoir in South Iraq by Combining FZI with NMR. In Proceedings of the SPWLA Asia-Pacific Regional Conference, Bangkok, Thailand, 1–4 March 2020; OnePetro: Richardson, TX, USA, 2020.
13. Trevizan, W.; Coutinho, B.; Netto, P.; Rios, E.; Ramos, P.; Salazar, J.; Bressan, M. Magnetic Resonance (NMR) Approach for Permeability Estimation in Carbonate Rocks. In *Proceedings of the OTC Brasil*; OnePetro: Richardson, TX, USA, 2015.
14. Davis, J.M.; Roy, N.D.; Mozley, P.S.; Hall, J.S. The Effect of Carbonate Cementation on Permeability Heterogeneity in Fluvial Aquifers: An Outcrop Analog Study. *Sediment. Geol.* **2006**, *184*, 267–280. [CrossRef]
15. Dou, Q.; Sun, Y.; Sullivan, C. Rock-Physics-Based Carbonate Pore Type Characterization and Reservoir Permeability Heterogeneity Evaluation, Upper San Andres Reservoir, Permian Basin, West Texas. *J. Appl. Geophys.* **2011**, *74*, 8–18. [CrossRef]
16. Corbett, P.W.M.; Wang, H.; Câmara, R.N.; Tavares, A.C.; Borghi de Almeida, L.F.; Perosi, F.; Machado, A.; Jiang, Z.; Ma, J.; Bagueira, R. Using the Porosity Exponent (m) and Pore-Scale Resistivity Modelling to Understand Pore Fabric Types in Coquinas (Barremian-Aptian) of the Morro Do Chaves Formation, NE Brazil. *Mar. Pet. Geol.* **2017**, *88*, 628–647. [CrossRef]
17. Ehrenberg, S.N.; Nadeau, P.H. Sandstone vs. Carbonate Petroleum Reservoirs: A Global Perspective on Porosity-Depth and Porosity-Permeability Relationships. *AAPG Bull.* **2005**, *89*, 435–445. [CrossRef]
18. Harju, J.A.; Malki, M.L.; Rasouli, V. Effect of Mineralogy on Elastic Properties of the Bakken Formation: A Lab Scale Rock Physics Modelling. *Geoenergy Sci. Eng.* **2023**, *224*, 211487. [CrossRef]

19. Hulea, I.N.; Nicholls, C.A. Carbonate Rock Characterization and Modeling: Capillary Pressure and Permeability in Multimodal Rocks—A Look beyond Sample Specific Heterogeneity. *AAPG Bull.* **2012**, *96*, 1627–1642. [CrossRef]
20. Makhloufi, Y.; Collin, P.-Y.; Bergerat, F.; Casteleyn, L.; Claes, S.; David, C.; Menendez, B.; Monna, F.; Robion, P.; Sizun, J.-P.; et al. Impact of Sedimentology and Diagenesis on the Petrophysical Properties of a Tight Oolitic Carbonate Reservoir. The Case of the *Oolithe Blanche Formation* (Bathonian, Paris Basin, France). *Mar. Pet. Geol.* **2013**, *48*, 323–340. [CrossRef]
21. Matonti, C.; Guglielmi, Y.; Viseur, S.; Bruna, P.O.; Borgomano, J.; Dahl, C.; Marié, L. Heterogeneities and Diagenetic Control on the Spatial Distribution of Carbonate Rocks Acoustic Properties at the Outcrop Scale. *Tectonophysics* **2015**, *638*, 94–111. [CrossRef]
22. He, J.; Ding, W.; Li, A.; Sun, Y.; Dai, P.; Yin, S.; Chen, E.; Gu, Y. Quantitative Microporosity Evaluation Using Mercury Injection and Digital Image Analysis in Tight Carbonate Rocks: A Case Study from the Ordovician in the Tazhong Palaeouplift, Tarim Basin, NW China. *J. Nat. Gas. Sci. Eng.* **2016**, *34*, 627–644. [CrossRef]
23. Hollis, C. Diagenetic Controls on Reservoir Properties of Carbonate Successions within the Albian–Turonian of the Arabian Plate. *Pet. Geosci.* **2011**, *17*, 223–241. [CrossRef]
24. Rong, H.; Jiao, Y.; Wu, L.; Gu, Y.; Zhang, L.; Li, R.; Zeng, F. Effects of Diagenesis on the Acoustic Velocity of the Triassic Oolitic Shoals in the Yudongzi Outcrop of Erlangmiao Area, Northwest Sichuan Basin. *J. Earth Sci.* **2012**, *23*, 542–558. [CrossRef]
25. Wilson, M.E.J.; Evans, M.J. Sedimentology and Diagenesis of Tertiary Carbonates on the Mangkalihat Peninsula, Borneo: Implications for Subsurface Reservoir Quality. *Mar. Pet. Geol.* **2002**, *19*, 873–900. [CrossRef]
26. Bultreys, T.; Van Hoorebeke, L.; Cnudde, V. Multi-Scale, Micro-Computed Tomography-Based Pore Network Models to Simulate Drainage in Heterogeneous Rocks. *Adv. Water Resour.* **2015**, *78*, 36–49. [CrossRef]
27. Kallel, W.; van Dijke, M.I.J.; Sorbie, K.S.; Wood, R.; Jiang, Z.; Harland, S. Modelling the Effect of Wettability Distributions on Oil Recovery from Microporous Carbonate Reservoirs. *Adv. Water Resour.* **2016**, *95*, 317–328. [CrossRef]
28. Mehmani, A.; Prodanović, M. The Effect of Microporosity on Transport Properties in Porous Media. *Adv. Water Resour.* **2014**, *63*, 104–119. [CrossRef]
29. Pak, T.; Butler, I.B.; Geiger, S.; Van Dijke, M.I.J.; Jiang, Z.; Surmas, R. Multiscale Pore-network Representation of Heterogeneous Carbonate Rocks. *Water Resour. Res.* **2016**, *52*, 5433–5441. [CrossRef]
30. Payne, S.S.; Wild, P.; Lubbe, R. An Integrated Solution to Rock Physics Modelling in Fractured Carbonate Reservoirs. In *SEG Technical Program Expanded Abstracts 2010*; SEG Technical Program Expanded Abstracts; Society of Exploration Geophysicists: Tokyo, Japan, 2010; pp. 358–362.
31. Harland, S.R.; Wood, R.A.; Curtis, A.; Van Dijke, M.I.J.; Stratford, K.; Jiang, Z.; Kallel, W.; Sorbie, K. Quantifying Flow in Variably Wet Microporous Carbonates Using Object-Based Geological Modeling and Both Lattice-Boltzmann and Pore-Network Fluid Flow Simulations. *AAPG Bull.* **2015**, *99*, 1827–1860. [CrossRef]
32. Wang Tectonic Evolution of the Western Kunlun Orogenic Belt, Western China. *J. Asian Earth Sci.* **2004**, *24*, 153–161. [CrossRef]
33. Choquette, P.W.; Pray, L.C. Geologic Nomenclature and Classification of Porosity in Sedimentary Carbonates. *AAPG Bull.* **1970**, *54*, 207–250. [CrossRef]
34. Skalinski, M.; Kenter, J.A.M. Carbonate Petrophysical Rock Typing: Integrating Geological Attributes and Petrophysical Properties While Linking with Dynamic Behaviour. *Geol. Soc. Lond. Spec. Publ.* **2015**, *406*, 229–259. [CrossRef]
35. Cerepi, A.; Durand, C.; Brosse, E. Pore Microgeometry Analysis in Low-Resistivity Sandstone Reservoirs. *J. Pet. Sci. Eng.* **2002**, *35*, 205–232. [CrossRef]
36. Malki, M.L.; Saberi, M.R.; Kolawole, O.; Rasouli, V.; Sennaoui, B.; Ozotta, O. Underlying Mechanisms and Controlling Factors of Carbonate Reservoir Characterization from Rock Physics Perspective: A Comprehensive Review. *Geoenergy Sci. Eng.* **2023**, *226*, 211793. [CrossRef]
37. Sok, R.M.; Knackstedt, M.A.; Varslot, T.; Ghous, A.; Latham, S.; Sheppard, A.P. Pore Scale Characterization of Carbonates at Multiple Scales: Integration of Micro-CT, BSEM, and FIBSEM. *Petrophysics-SPWLA J. Form. Eval. Reserv. Descr.* **2010**, *51*..
38. Verwer, K.; Eberli, G.P.; Weger, R.J. Effect of Pore Structure on Electrical Resistivity in Carbonates. *AAPG Bull.* **2011**, *95*, 175–190. [CrossRef]
39. Kesserwan, H.; Jin, G.; Agrawal, G. Wettability and Pore Structure Characterization of Laminated Carbonate Source Rocks. In *Proceedings of the SPE Middle East Oil & Gas Show and Conference*; OnePetro: Richardson, TX, USA, 2017.
40. Pramana, A.A.; Ray, D.R.M.; Latief, F.D.E.; Gibrata, M.A. Relative Permeability from Digital Analysis of a Carbonate Synthetic Core. *J. Phys. Conf. Ser.* **2022**, *2243*, 12022. [CrossRef]
41. Rozhko, A.Y.; Lozovyi, S.; Naumann, M.; Hansteen, F.; Ravasi, M. Stimulating Relative Permeability Changes by Low-Frequency Elastic Waves: Theory and Lab Experiments. *J. Pet. Sci. Eng.* **2022**, *215*, 110393. [CrossRef]
42. Yao, J.; Hu, R.; Wang, C.; Yang, Y. Multiscale Pore Structure Analysis in Carbonate Rocks. *Int. J. Multiscale Comput. Eng.* **2015**, *13*, 1–9. [CrossRef]
43. Oyewole, E.; Saneifar, M.; Heidari, Z. Multi-Scale Characterization of Pore Structure in Carbonate Formations: Application to the Sacroc Unit. In *Proceedings of the SPWLA 56th Annual Logging Symposium, Long Beach, CA, USA, 18–22 July 2015*; OnePetro: Richardson, TX, USA, 2015.

44. Wang, C.; Yao, J.; Wu, K.; Yang, Y.; Wang, X. Pore-Scale Characterization of Carbonate Rock Heterogeneity and Prediction of Petrophysical Properties. In Proceedings of the 2012 International Symposium of the Society of Core Analysts, Aberdeen, UK, 27–30 August 2012.
45. Oyewole, E.; Saneifar, M.; Heidari, Z. Multiscale Characterization of Pore Structure in Carbonate Formations: Application to the Scurry Area Canyon Reef Operators Committee Unit. *Interpretation* **2016**, *4*, SF165–SF177. [CrossRef]
46. Zhenpeng, L.; Weifeng, L.; Desheng, M.; Qingjie, L.; Ninghong, J.; Tong, L.; Xu, J.; Danyong, L. Characterization of Pore Structure in Tight Oil Reservoir Rock. In *Proceedings of the SPE/IATMI Asia Pacific Oil & Gas Conference and Exhibition*; SPE: Nusa Dua, Bali, Indonesia, 2015; p. SPE-176358-MS.
47. Yao, Y.; Liu, D. Comparison of Low-Field NMR and Mercury Intrusion Porosimetry in Characterizing Pore Size Distributions of Coals. *Fuel* **2012**, *95*, 152–158. [CrossRef]
48. Xiao, P.F.; Yang, Z.M.; Zhang, Y.P.; Gai, C.C. Study on Micro Pore Structure Characteristics of Carbonate Cores of Low Permeability. *Adv. Mater. Res.* **2014**, *1015*, 129–134. [CrossRef]
49. Yue, H.; Liu, H.; Hua, H.; Han, J.; Wang, F. Comprehensive Pore Structure Characterization and Permeability Prediction of Carbonate Reservoirs Using High-Pressure Mercury Intrusion and X-Ray CT. *Carbonates Evaporites* **2024**, *39*, 18. [CrossRef]
50. Mahmoud, A.; Gajbhiye, R.; Li, J.; Dvorkin, J.; Hussaini, S.R.; AlMukainah, H.S. Digital Rock Physics (DRP) Workflow to Assess Reservoir Flow Characteristics. *Arab. J. Geosci.* **2023**, *16*, 248. [CrossRef]
51. Basso, M.; Belila, A.M.P.; Chinelatto, G.F.; Souza, J.P.d.P.; Vidal, A.C. Sedimentology and Petrophysical Analysis of Pre-Salt Lacustrine Carbonate Reservoir from the Santos Basin, Southeast Brazil. *Int. J. Earth Sci.* **2021**, *110*, 2573–2595. [CrossRef]
52. Iraji, S.; Soltanmohammadi, R.; Matheus, G.F.; Basso, M.; Vidal, A.C. Application of Unsupervised Learning and Deep Learning for Rock Type Prediction and Petrophysical Characterization Using Multi-Scale Data. *Geoenergy Sci. Eng.* **2023**, *230*, 212241. [CrossRef]
53. Radwan, A.E.; Trippetta, F.; Kassem, A.A.; Kania, M. Multi-Scale Characterization of Unconventional Tight Carbonate Reservoir: Insights from October Oil Filed, Gulf of Suez Rift Basin, Egypt. *J. Pet. Sci. Eng.* **2021**, *197*, 107968. [CrossRef]
54. Baouche, R.; Sen, S.; Ganguli, S.S.; Boutaleb, K. Petrophysical and Geomechanical Characterization of the Late Cretaceous Limestone Reservoirs from the Southeastern Constantine Basin, Algeria. *Interpretation* **2021**, *9*, SH1–SH9. [CrossRef]
55. Razavifar, M.; Mukhametdinova, A.; Nikooee, E.; Burukhin, A.; Rezaei, A.; Cheremisin, A.; Riazi, M. Rock Porous Structure Characterization: A Critical Assessment of Various State-of-the-Art Techniques. *Transp. Porous Media* **2021**, *136*, 431–456. [CrossRef]
56. Anovitz, L.M.; Freiburg, J.T.; Wasbrough, M.; Mildner, D.F.R.; Littrell, K.C.; Pipich, V.; Ilavsky, J. The Effects of Burial Diagenesis on Multiscale Porosity in the St. Peter Sandstone: An Imaging, Small-Angle, and Ultra-Small-Angle Neutron Scattering Analysis. *Mar. Pet. Geol.* **2018**, *92*, 352–371. [CrossRef]
57. Chalmers, G.R.; Bustin, R.M.; Power, I.M. Characterization of Gas Shale Pore Systems by Porosimetry, Pycnometry, Surface Area, and Field Emission Scanning Electron Microscopy/Transmission Electron Microscopy Image Analyses: Examples from the Barnett, Woodford, Haynesville, Marcellus, and Doig Units. *AAPG Bull.* **2012**, *96*, 1099–1119. [CrossRef]
58. Gu, X.; Cole, D.R.; Rother, G.; Mildner, D.F.R.; Brantley, S.L. Pores in Marcellus Shale: A Neutron Scattering and FIB-SEM Study. *Energy Fuels* **2015**, *29*, 1295–1308. [CrossRef]
59. Menke, H.P.; Andrew, M.G.; Blunt, M.J.; Bijeljic, B. Reservoir Condition Imaging of Reactive Transport in Heterogeneous Carbonates Using Fast Synchrotron Tomography—Effect of Initial Pore Structure and Flow Conditions. *Chem. Geol.* **2016**, *428*, 15–26. [CrossRef]
60. Nie, B.; Liu, X.; Yang, L.; Meng, J.; Li, X. Pore Structure Characterization of Different Rank Coals Using Gas Adsorption and Scanning Electron Microscopy. *Fuel* **2015**, *158*, 908–917. [CrossRef]
61. Tang, X.; Jiang, Z.; Jiang, S.; Li, Z. Heterogeneous Nanoporosity of the Silurian Longmaxi Formation Shale Gas Reservoir in the Sichuan Basin Using the QEMSCAN, FIB-SEM, and Nano-CT Methods. *Mar. Pet. Geol.* **2016**, *78*, 99–109. [CrossRef]
62. Yan, Z.; Chen, C.; Fan, P.; Wang, M.; Fang, X. Pore Structure Characterization of Ten Typical Rocks in China. *Electron. J. Geotech. Eng.* **2015**, *20*, 479–494.
63. Zambrano, M.; Tondi, E.; Mancini, L.; Arzilli, F.; Lanzafame, G.; Materazzi, M.; Torrieri, S. 3D Pore-Network Quantitative Analysis in Deformed Carbonate Grainstones. *Mar. Pet. Geol.* **2017**, *82*, 251–264. [CrossRef]
64. Gane, P.A.C.; Ridgway, C.J.; Lehtinen, E.; Valiullin, R.; Furó, I.; Schoelkopf, J.; Paulapuro, H.; Daicic, J. Comparison of NMR Cryoporometry, Mercury Intrusion Porosimetry, and DSC Thermoporosimetry in Characterizing Pore Size Distributions of Compressed Finely Ground Calcium Carbonate Structures. *Ind. Eng. Chem. Res.* **2004**, *43*, 7920–7927. [CrossRef]
65. Jia, M.; Huang, W.; Li, Y. Quantitative Characterization of Pore Structure Parameters in Coal Based on Image Processing and SEM Technology. *Energies* **2023**, *16*, 1663. [CrossRef]
66. Zhang, S.; Klimentidis, R.E.; Barthelemy, P. 2011: Porosity and Permeability Analysis on Nanoscale Fib-Sem 3D Imaging of Shale Rock. In Proceedings of the 2011 International Symposium of the Society of Core Analysts, Austin, TX, USA, 18–21 September 2011.

67. Zhang, Y.; Ghanbarnezhad Moghanloo, R.; Davudov, D. Pore Structure Characterization of a Shale Sample Using SEM Images. In *Proceedings of the SPE Western Regional Meeting*; SPE: San Jose, CA, USA, 2019; p. D032S002R004.
68. Bakshi, T.; Prusty, B.K.; Pathak, K.; Nayak, B.R.; Mani, D.; Pal, S.K. Source Rock Characteristics and Pore Characterization of Indian Shale. *J. Nat. Gas Sci. Eng.* **2017**, *45*, 761–770. [CrossRef]
69. Clarkson, C.R.; Solano, N.; Bustin, R.M.; Bustin, A.M.M.; Chalmers, G.R.L.; He, L.; Melnichenko, Y.B.; Radliński, A.P.; Blach, T.P. Pore Structure Characterization of North American Shale Gas Reservoirs Using USANS/SANS, Gas Adsorption, and Mercury Intrusion. *Fuel* **2013**, *103*, 606–616. [CrossRef]
70. Faÿ-Gomord, O.; Soete, J.; Katika, K.; Galaup, S.; Caline, B.; Descamps, F.; Lasseur, E.; Fabricius, I.L.; Saïag, J.; Swennen, R.; et al. New Insight into the Microtexture of Chalks from NMR Analysis. *Mar. Pet. Geol.* **2016**, *75*, 252–271. [CrossRef]
71. Bulygin, F.V.; Lyaskovskii, V.L. An Investigation of Methods of Measuring the Diameter of the Electron Probe of Scanning Electron Microscopes Using Modern Nanometer Band Standard Measures. *Meas. Tech.* **2010**, *53*, 996–1001. [CrossRef]
72. Mohammed Sajed, O.K.; Glover, P.W.J. Dolomitisation, Cementation and Reservoir Quality in Three Jurassic and Cretaceous Carbonate Reservoirs in North-Western Iraq. *Mar. Pet. Geol.* **2020**, *115*, 104256. [CrossRef]
73. Wandrol, P.; Matějková, J.; Rek, A. High Resolution Imaging by Means of Backscattered Electrons in the Scanning Electron Microscope. *Mater. Sci. Forum* **2008**, *567–568*, 313–316. [CrossRef]
74. Liu, Z.; Bai, S.; Burke, S.; Burrow, J.N.; Geurts, R.; Huang, C.-J.; Jiao, C.; Lee, H.-B.; Meng, Y.S.; Novák, L.; et al. FIB-SEM: Emerging Multimodal/Multiscale Characterization Techniques for Advanced Battery Development. *Chem. Rev.* **2025**, *125*, 5228–5281. [CrossRef]
75. Golsanami, N.; Kadkhodaie-Ilkhchi, A.; Sharghi, Y.; Zeinali, M. Estimating NMR T2 Distribution Data from Well Log Data with the Use of a Committee Machine Approach: A Case Study from the Asmari Formation in the Zagros Basin, Iran. *J. Pet. Sci. Eng.* **2014**, *114*, 38–51. [CrossRef]
76. Li, A.; Ding, W.; Wang, R.; He, J.; Wang, X.; Sun, Y.; Gu, Y.; Jiao, N. Petrophysical Characterization of Shale Reservoir Based on Nuclear Magnetic Resonance (NMR) Experiment: A Case Study of Lower Cambrian Qiongzhusi Formation in Eastern Yunnan Province, South China. *J. Nat. Gas. Sci. Eng.* **2017**, *37*, 29–38. [CrossRef]
77. Testamanti, M.N.; Rezaee, R. Determination of NMR T2 Cut-off for Clay Bound Water in Shales: A Case Study of Carynginia Formation, Perth Basin, Western Australia. *J. Pet. Sci. Eng.* **2017**, *149*, 497–503. [CrossRef]
78. Zhang, L.; Lu, S.; Xiao, D.; Gu, M. Characterization of Full Pore Size Distribution and Its Significance to Macroscopic Physical Parameters in Tight Glutenites. *J. Nat. Gas. Sci. Eng.* **2017**, *38*, 434–449. [CrossRef]
79. Zhang, P.; Lu, S.; Li, J.; Chen, C.; Xue, H.; Zhang, J. Petrophysical Characterization of Oil-Bearing Shales by Low-Field Nuclear Magnetic Resonance (NMR). *Mar. Pet. Geol.* **2018**, *89*, 775–785. [CrossRef]
80. Zhang, Y.; Xiao, L.; Liao, G.; Song, Y.-Q. Direct Correlation of Diffusion and Pore Size Distributions with Low Field NMR. *J. Magn. Reson.* **2016**, *269*, 196–202. [CrossRef]
81. Zhou, L.; Kang, Z. Fractal Characterization of Pores in Shales Using NMR: A Case Study from the Lower Cambrian Niutitang Formation in the Middle Yangtze Platform, Southwest China. *J. Nat. Gas Sci. Eng.* **2016**, *35*, 860–872. [CrossRef]
82. Arns, C.H. A Comparison of Pore Size Distributions Derived by NMR and X-Ray-CT Techniques. *Phys. A* **2004**, *339*, 159–165. [CrossRef]
83. Hugh Daigle Determining Fractal Dimension from Nuclear Magnetic Resonance Data in Rocks with Internal Magnetic Field Gradients | GEOPHYSICS. *Geophysics* **2014**, *79*, D425–D431. [CrossRef]
84. Kleinberg, R.L.; Farooqui, S.A.; Horsfield, M.A. $T1/T2$ Ratio and Frequency Dependence of NMR Relaxation in Porous Sedimentary Rocks. *J. Colloid Interface Sci.* **1993**, *158*, 195–198. [CrossRef]
85. Li, S.; Tang, D.; Xu, H.; Yang, Z. Advanced Characterization of Physical Properties of Coals with Different Coal Structures by Nuclear Magnetic Resonance and X-Ray Computed Tomography. *Comput. Geosci.* **2012**, *48*, 220–227. [CrossRef]
86. Tan, M.; Mao, K.; Song, X.; Yang, X.; Xu, J. NMR Petrophysical Interpretation Method of Gas Shale Based on Core NMR Experiment. *J. Pet. Sci. Eng.* **2015**, *136*, 100–111. [CrossRef]
87. Xu, L.; Cai, M.; Dai, Z.; Zheng, Z.; Chen, W.; Yin, S.; Zhang, X.; Thanh, H.V.; Soltanian, M.R. Fractal and NMR Based Characterizations of Multi-Scale Pore Structure Alterations in Tight Sandstones Due to $scCO_2$-Water–Rock Interactions. *Chem. Eng. J.* **2025**, *508*, 160898. [CrossRef]
88. Yin, P.; Song, H.; Ma, H.; Yang, W.; He, Z.; Zhu, X. The Modification of the Kozeny-Carman Equation through the Lattice Boltzmann Simulation and Experimental Verification. *J. Hydrol.* **2022**, *609*, 127738. [CrossRef]
89. Arismendi Florez, J.J.; Ferrari, J.V.; Ulsen, C. Study of the Contact Angle and Roughness Effects on Mercury Intrusion Porosimetry (MIP) Analysis in Natural/Real Carbonate Rocks Using Massive Pure Minerals and Synthetic Carbonate Rocks. *J. Mater. Res. Technol.* **2024**, *32*, 286–317. [CrossRef]
90. Feng, G.; Zhang, L.; Yan, J.; Chen, S.; Pu, X.; Han, W.; Shi, Z.; Zhang, W. Lithofacies-Based Analysis of Pore Structure Characteristics and Controlling Factors of Shale Reservoirs: A Case Study of the Second Member of the Kongdian Formation in the Cangdong Sag, Bohai Bay Basin, China. *Mar. Pet. Geol.* **2025**, *182*, 107575. [CrossRef]

91. Hu, Q.; Zhang, Y.; Meng, X.; Li, Z.; Xie, Z.; Li, M. Characterization of Micro-Nano Pore Networks in Shale Oil Reservoirs of Paleogene Shahejie Formation in Dongying Sag of Bohai Bay Basin, East China. *Pet. Explor. Dev.* **2017**, *44*, 720–730. [CrossRef]
92. Guo, X.; Huang, Z.; Zhao, L.; Han, W.; Ding, C.; Sun, X.; Yan, R.; Zhang, T.; Yang, X.; Wang, R. Pore Structure and Multi-Fractal Analysis of Tight Sandstone Using MIP, NMR and NMRC Methods: A Case Study from the Kuqa Depression, China. *J. Pet. Sci. Eng.* **2019**, *178*, 544–558. [CrossRef]
93. He, R.; Nantung, T.; Lu, N. (Luna) Unraveling Microstructural Evolution in Air-Entrained Mortar and Paste: Insights from MIP and Micro-CT Tomography amid Cyclic Freezing-Thawing Damage. *J. Build. Eng.* **2024**, *94*, 109922. [CrossRef]
94. Hou, X.; Qi, S.; Guo, S.; Zhang, L.; Ma, L.; Li, Y.; Wang, Y.; Li, T.; Peng, J. Three-Dimensional Pore Structure Characteristics of Intact and Compacted Loess and Their Controls on Hydraulic Permeability. *J. Hydrol.* **2025**, *663*, 134126. [CrossRef]
95. Xiong, Q.; Baychev, T.G.; Jivkov, A.P. Review of Pore Network Modelling of Porous Media: Experimental Characterisations, Network Constructions and Applications to Reactive Transport. *J. Contam. Hydrol.* **2016**, *192*, 101–117. [CrossRef]
96. Lai, J.; Wang, G.; Wang, Z.; Chen, J.; Pang, X.; Wang, S.; Zhou, Z.; He, Z.; Qin, Z.; Fan, X. A Review on Pore Structure Characterization in Tight Sandstones. *Earth Sci. Rev.* **2018**, *177*, 436–457. [CrossRef]
97. Li, X.; Kang, Y.; Haghighi, M. Investigation of Pore Size Distributions of Coals with Different Structures by Nuclear Magnetic Resonance (NMR) and Mercury Intrusion Porosimetry (MIP). *Measurement* **2018**, *116*, 122–128. [CrossRef]
98. You, L.; Tan, Q.; Kang, Y.; Xu, C.; Lin, C. Reconstruction and Prediction of Capillary Pressure Curve Based on Particle Swarm Optimization-Back Propagation Neural Network Method. *Petroleum* **2018**, *4*, 268–280. [CrossRef]
99. Mishra, V.K.; Mendhe, V.A.; Kamble, A.D.; Pandey, S.; Singh, V.P.; Shukla, P. Significance of Organo-Mineralogical Constituents on Pore Distribution, Fractals and Gas Sorption Mechanism of Permian Shale Beds in Korba Sub-Basin of the Son-Mahanadi Valley, India. *Geoenergy Sci. Eng.* **2023**, *231*, 212334. [CrossRef]
100. Yuan, X.; Hu, Q.; Lin, X.; Zhao, C.; Wang, Q.; Tachi, Y.; Fukatsu, Y.; Hamamoto, S.; Siitari-Kauppi, M.; Li, X. Pore Connectivity Influences Mass Transport in Natural Rocks: Pore Structure, Gas Diffusion and Batch Sorption Studies. *J. Hydrol.* **2023**, *618*, 129172. [CrossRef]
101. Jiao, K.; Yao, S.; Zhang, K.; Hu, W.; Cao, J. The Evolution of Nanopores and Surface Roughness in Naturally Matured Coals in South China: An Atomic Force Microscopy and Image Processing Study. *Fuel* **2018**, *234*, 1123–1131. [CrossRef]
102. Medina-Rodriguez, B.X.; Alvarado, V. Use of Gas Adsorption and Inversion Methods for Shale Pore Structure Characterization. *Energies* **2021**, *14*, 2880. [CrossRef]
103. Xiong, S.; Gao, Z.; Wei, W.; Wang, Y. Differential Effects of Pore Structure of Mineral and Maceral Components on the Methane Adsorption Capacity Evolution of the Lower Jurassic Da'anzhai Member of the Ziliujing Formation Lacustrine Shale, Sichuan Basin, China. *Mar. Pet. Geol.* **2023**, *147*, 106017. [CrossRef]
104. Cai, H.; Zhang, Q.; Ye, G.; Lu, L.; Wu, C.; Ji, F. Investigation on Strong Vertical Permeability and Micro-Pore Characteristics of Jinan Red Clay Using X-Ray Micro-Tomography. *Environ. Earth Sci.* **2023**, *82*, 122. [CrossRef]
105. Song, R.; Wang, Y.; Sun, S.; Liu, J. Characterization and Microfabrication of Natural Porous Rocks: From Micro-CT Imaging and Digital Rock Modelling to Micro-3D-Printed Rock Analogs. *J. Pet. Sci. Eng.* **2021**, *205*, 108827. [CrossRef]
106. Korat, L.; Ducman, V.; Legat, A.; Mirtič, B. Characterisation of the Pore-Forming Process in Lightweight Aggregate Based on Silica Sludge by Means of X-Ray Micro-Tomography (Micro-CT) and Mercury Intrusion Porosimetry (MIP). *Ceram. Int.* **2013**, *39*, 6997–7005. [CrossRef]
107. Su, Y.; Zha, M.; Jiang, L.; Ding, X.; Qu, J.; Jin, J.; Iglauer, S. Pore Structure and Fluid Distribution of Tight Sandstone by the Combined Use of SEM, MICP and X-Ray Micro-CT. *J. Pet. Sci. Eng.* **2022**, *208*, 109241. [CrossRef]
108. Li, W. Pore-Throat Structure Characteristics and Its Impact on the Porosity and Permeability Relationship of Carboniferous Carbonate Reservoirs in Eastern Edge of Pre-Caspian Basin. *Pet. Explor. Dev.* **2020**, *47*, 1027–1041. [CrossRef]
109. Duan, W.; Zhiqian, G.; Tailiang, F.; Miaomiao, M.; Yue, C.; Yangbing, L.; Chenjia, Z. New Insight into the Characteristics of Tight Carbonate Based on Nuclear Magnetic Resonance. *Energy Fuels* **2018**, *32*, 2962–2972. [CrossRef]
110. Tan, Q.; Kang, Y.; You, L.; Xu, F.; Meng, S. A Comprehensive Insight into the Multiscale Pore Structure Characterization of Saline-Lacustrine Tight Carbonate Reservoir. *J. Pet. Sci. Eng.* **2020**, *187*, 106744. [CrossRef]
111. Belfield, W.C. Characterization of a Naturally Fractured Carbonate Reservoir: Lisburne Field, Prudhoe Bay, Alaska. In *Proceedings of the SPE Annual Technical Conference and Exhibition*; SPE: Houston, TX, USA, 1988; p. SPE-18174-MS.
112. Huang, C.; Zhao, F.; Yuan, J.; Wu, L.; Gengxin, C. The Characteristics of Dolomite Reservoir in Saline Lacustrine Basin, Qaidam, China. *Carbonates Evaporites* **2016**, *31*, 307–317. [CrossRef]
113. Zhang, Y.; Yang, S.; Zhang, Z.; Li, Q.; Deng, H.; Chen, J.; Geng, W.; Wang, M.; Chen, Z.; Chen, H. Multiscale Pore Structure Characterization of an Ultra-Deep Carbonate Gas Reservoir. *J. Pet. Sci. Eng.* **2022**, *208*, 109751. [CrossRef]
114. Zhang, Y. Comparative Study of Pore Structure Characterization for Different Rock Samples Using Digital Images. Master's Thesis, University of Oklahoma, Norman, OK, USA, 2019.
115. Al-Kharusi, A.S.; Blunt, M.J. Network Extraction from Sandstone and Carbonate Pore Space Images. *J. Pet. Sci. Eng.* **2007**, *56*, 219–231. [CrossRef]

116. Okabe, H.; Blunt, M.J. Prediction of Permeability for Porous Media Reconstructed Using Multiple-Point Statistics. *Phys. Rev. E* **2004**, *70*, 66135. [CrossRef]
117. Wang, L.; He, Y.; Peng, X.; Deng, H.; Liu, Y.; Xu, W. Pore Structure Characteristics of an Ultradeep Carbonate Gas Reservoir and Their Effects on Gas Storage and Percolation Capacities in the Deng IV Member, Gaoshiti-Moxi Area, Sichuan Basin, SW China. *Mar. Pet. Geol.* **2020**, *111*, 44–65. [CrossRef]
118. Wang, M.; Guo, J.; Zhou, Y. Determination of NMR T2 Cutoff and CT Scanning for Pore Structure Evaluation in Mixed Siliciclastic–Carbonate Rocks Before and After Acidification. Available online: https://www.mdpi.com/1996-1073/13/6/1338 (accessed on 16 July 2025).
119. Genty, C.; Jensen, J.L.; Ahr, W.M. Distinguishing Carbonate Reservoir Pore Facies with Nuclear Magnetic Resonance Measurements. *Nat. Resour. Res.* **2007**, *16*, 45–54. [CrossRef]
120. Tian, F.; Wang, W.; Liu, N.; Jiang, J.; Niu, C.; Zhang, Y.; Li, Y. Rock-Type Definition and Pore Characterization of Tight Carbonate Rocks Based on Thin Sections and MICP and NMR Experiments. *Appl. Magn. Reson.* **2018**, *49*, 631–652. [CrossRef]